J Mater Sci (2017) 52:9739–9763

Energy materials

Exploring electronic properties and NO gas sensitivity of Si-doped SW-BNNTs under axial tensile strain

Hossein Roohi[1,*], Layla Maleki[1], and Maryam Erfani Moradzadeh[1]

[1] *Department of Chemistry, Faculty of Science, University of Guilan, Rasht, Iran*

Received: 2 February 2017
Accepted: 26 April 2017
Published online: 9 May 2017

ABSTRACT

Continuously tuning electronic and magnetic properties of nanomaterials specially by applying an axial tensile strain is a promising route for construction of impending electronic and optoelectronic nanodevices. In the present work, Si doping and axial tensile strain were simultaneously utilized in exploring the structural and electronic properties of single-walled (6,0) $\mathbf{Si_N}$, $\mathbf{Si_B}$ and $\mathbf{Si_{N,B}}$-doped Stone–Wales defective boron nitride nanotubes at M05-2X/6–31+G(d) level. Our findings demonstrate that the Si doping of SW-BNNT destroys the hexagonal BN network and alters the insulating feature of the SW-BNNT. Binding energies of Si-doped SW-BNNTs are estimated to be smaller than un-doped SW-BNNT and decrease continuously upon axial tensile strain. It can be estimated that the Si-doped SW–BNNTs and, in turn, their axial strained forms are more suitable than SW-BNNT one for photoconductivity applications. The unstrained $\mathbf{Si_{N,B}}$ has a lower band gap than unstrained $\mathbf{Si_N}$ and $\mathbf{Si_B}$. The results show that the axial tensile strain is not a suitable strategy to improve the conductivity of $\mathbf{Si_{N,B}}$, contrary to those found in $\mathbf{Si_N}$ and $\mathbf{Si_B}$. In the second part of this work, sensitivity of strained and unstrained Si-doped SW-BNNTs toward NO gas is evaluated. The results show that the chemical adsorption of NO is thermodynamically favored in both strained and unstrained forms. Among the Si-doped SW-BNNT–NO complexes, $\mathbf{Si_{N,B}}$**-ON1** and $\mathbf{Si_B}$**-NO2** complexes with adsorption energy of −32.7 and −33.3 kcal mol^{-1}, respectively, are thermodynamically more stable than other complexes. In addition, dispersion-corrected adsorption energies were evaluated at M05-2X-D3/6-31++G(d,p)//M05-2X/6–31+G(d) level of theory. The greatest charge transfer value and change in the band gap upon adsorption was predicted in all complexes. Thus, it is expected that Si-doped SW-BNNT could be a favorable NT for removing and sensing the NO gas.

Address correspondence to E-mail: hroohi@guilan.ac.ir

DOI 10.1007/s10853-017-1146-y

Introduction

BN nanotubes (BNNTs) were theoretically predicted in 1994 [1] and then were experimentally realized in the following year. [2] The honeycomb arrangement of BNNT is similar to carbon nanotube (CNT), but B and N atoms completely substitute for C atoms. Contrary to CNTs that can be a semiconductor or a metallic nanostructured materials, BNNTs are electrical insulator materials with a constant band gap around 5.5 eV and almost independent of their radius and tube chirality. [3–5] This property has been primarily interested in studying the properties of BNNTs such as tuning the electronic properties. The chemical and physical methods can be utilized for tuning the electronic properties of BN nanotubes [6]. The physical methods include applying electric field [7] and strain [8], and the chemical methods contain doping, [9–20] introducing defect [21], functionalization [22, 23], absorption [24] and so on.

Kim et al. [25] have showed that the formation energy of a 2C-doped SW-BNNT is approximately 3.1 eV lower than that of the un-doped SW-BNNT having B–N bond. The NO adsorptions on the surface of C-doped SW-BNNTs are energetically favorable and are stronger than pristine and un-doped SW-BNNTs [24]. Due to the introduction of Pt states into the nanotube band gap, Pt-doped BNNTs are more reactive than pristine and SW defective BNNTs [26]. It has been reported that the adsorption of HCOH molecule on both Si-substituted boron defect site and Si-substituted nitrogen defect site of the BNNT is chemisorption, while its adsorption is predicted to be weak physisorption on the pristine BNNT. Besides, the Si-doped BNNT shows the high sensitivity to toxic HCOH [27].

The Stone–Wales (SW) transformation is a topological defect. Upon formation of this type of defect in BNNTs, B–B and N–N bonds are created and the formation of these bonds increases the total energy of the NT [28]. However, atomistic simulations [29, 30] and experiments [31, 32] have shown that the SW defect leads to the formation of 5–7 ring pairs in the hexagonal lattice of BNNTs. In addition, SW defect can be created in a BNNT under axial tension [32, 33].

The easy modifying of electronic properties of BNNTs is still a challenging task. The elastic strain engineering (ESE) is one of the nonchemical tools for adjusting the electronic properties. The ESE allows us to control the band gap of materials by simply applying an elastic strain. Effects of axial tension on the electronic properties of SW defective BNNTs were previously investigated [34–38]. Gupta et al. [39] were explored the impact of Si doping on the electronic structure and electron transport properties of boron nitride monolayers. Wei. et al. [40] have experimentally investigated the influence of tensile loading and pullouts on the properties of individual multiwalled BNNTs for the first time. Deformation behaviors of an (8,8) BNNT under axial tensile strains were investigated via molecular dynamics (MD) simulations by Liao et al. [41]. They reported that the BNNT starts to fail at the failure strain of 26.7%. The effect of axial tensile strain on structural and electronic properties of zigzag BNNT with different length and diameter was studied [8]. Ge et al. [42] found that the band gap of (n = odd number, 0) B_2C tubes decreases to zero by increasing tensile strain.

The study of the sensitivity of nanotubes toward different gases is at the center of deep experimental and theoretical researches [43, 44]. The Si-BNNTs were used as a metal-free catalyst for oxidation of NO [45]. Zhang et al. [46] fabricated a NO gas sensor employing multiwalled carbon nanotubes (MWCNTs). The adsorptions of CO and NO molecules on the surface of transition metals (V, Cr, Mn, Fe, Co or Ni)-doped (8,0) BNNTs were investigated by using first-principle calculations [47]. Moreover, SiC-based nanodevices were predicted to be useful for the design of the NO and CO sensors [48].

The effect of the Stone–Wales (SW) defect on the response of BNNT to axial tension was studied in our previous work [34]. In addition, we have investigated effect of C doping on the properties of SW-BNNTs [24]. In the first part of this work, the influences of simultaneously Si doping and axial tensile strain on electronic and structural properties of three $\mathbf{Si_N}$, $\mathbf{Si_B}$ and $\mathbf{Si_{N,B}}$-doped SW defective BNNTs are explored. To the best of our knowledge, no experimental or theoretical investigation has been reported on the sensitivity of strained and unstrained Si-doped SW defective BNNTs toward the NO gas. In the second part of the present work, reactivity and sensitivity of strained and unstrained Si-doped SW defective BNNTs toward NO gas were investigated.

Computational details

The DFT method was used to study the effect of axial tensile strain on the electronic and structural properties of Si-doped SW defective BNNTs. Three models of (6,0) zigzag single-walled Si-doped SW–BNNT consisting of $B_{35}N_{36}SiH_{12}$ (**Si_B**), $B_{36}N_{35}SiH_{12}$ (**Si_N**) and $B_{35}N_{35}Si_2H_{12}$ (**$Si_{N,B}$**) that the Si atoms are doped in the region of SW defect were explored. The structure NTs are shown in Fig. 1. All geometry

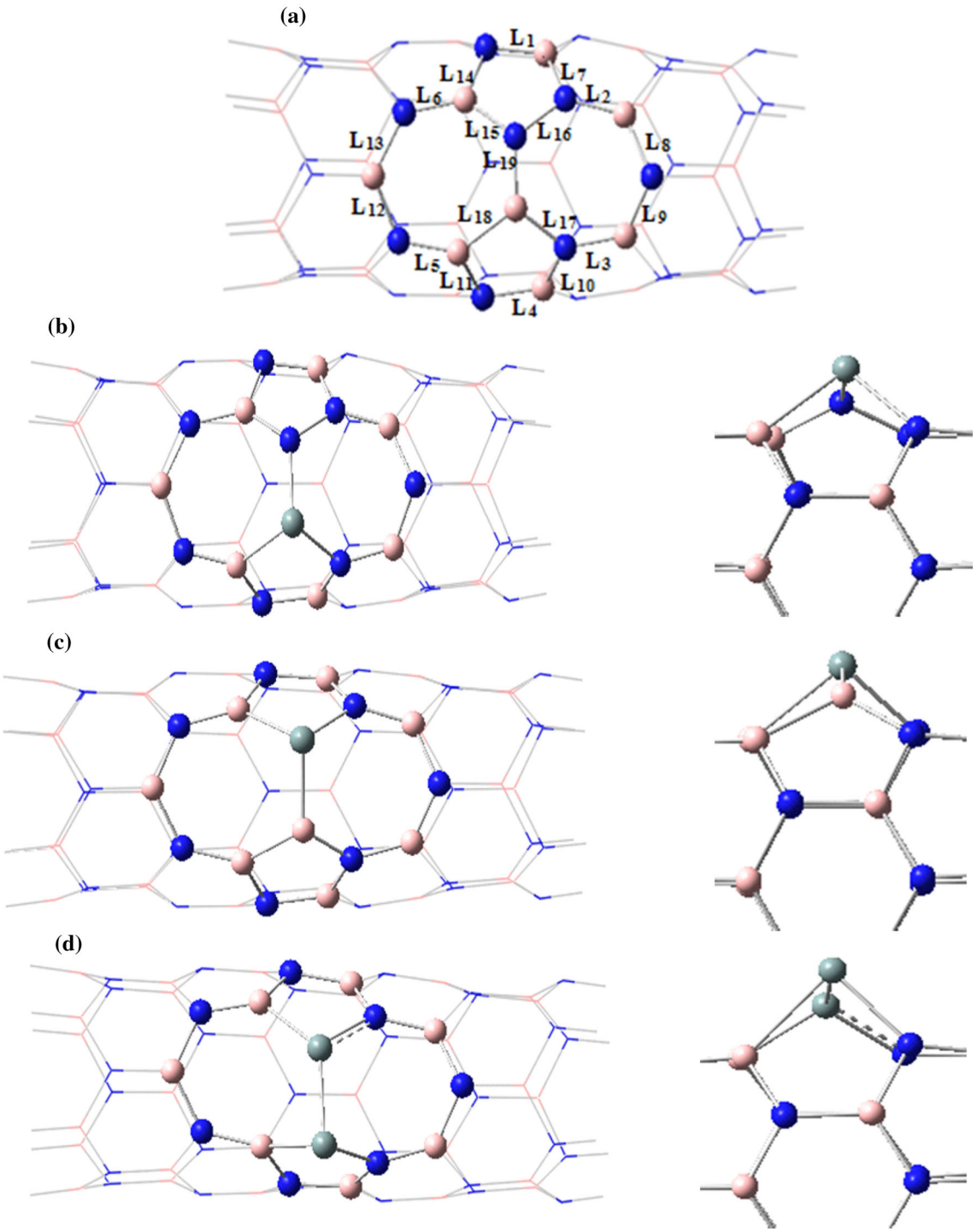

Figure 1 Optimized structures of **a** SW defective (6,0) BNNT, **b** $B_{35}N_{36}SiH_{12}$ (**Si_B**), **c** $B_{36}N_{35}SiH_{12}$ (**Si_N**) and **d** $B_{35}N_{35}Si_2H$ (**$Si_{N,B}$**). The B, N and Si atoms are represented in *pink*, *blue* and *silver*, respectively. The SW defects are *highlighted* in ball-stick representation.

optimizations were performed using the M05-2X functional [49, 50] and 6–31+G(d) basis set as implemented in the computer program packages [51, 52]. In the first step, the structures were optimized without any restriction. Then, the axial tensile strain is applied on optimized Si-doped SW–BNNT. No symmetric constraints are imposed during the optimization. In the axial stretching process, distances between B and N atoms at both ends of Si-doped SW–BNNT were scanned by 0.1 Å increments at nineteen steps and remaining degrees of freedom were relaxed during the calculations.

The binding energies (BE) per atom for Si-doped SW defective BNNTs are calculated according to the following formula:

$$\mathrm{BE} = \frac{[aE_{\mathrm{B}} + bE_{\mathrm{N}} + cE_{\mathrm{H}} + dE_{\mathrm{Si}}] - [E_{\mathrm{B}_a\mathrm{N}_b\mathrm{H}_c\mathrm{Si}_d}]}{a+b+c+d} \quad (1)$$

where a, b, c and d are the number of B, N, H and Si atoms. E_{B}, E_{N}, E_{H}, E_{Si} and $E_{\mathrm{B}_a\mathrm{N}_b\mathrm{H}_c\mathrm{Si}_d}$ e the ground state electronic energies of B, N, H, Si atoms and optimized doped BNNT, respectively. The engineering strain in the axial direction of the doped SW–BNNT is given [53] by

$$\varepsilon_{\mathrm{Eng}} = \frac{L - L_0}{L_0} \quad (2)$$

where L_0 is the initial length prior to loading and L is the nanotube length upon the strain.

The formation energies of the Si-doped SW defective BNNTs were estimated using Eq. (3) given below

$$E_{\mathrm{form}} = E_{\mathrm{d}} + (a+b)E_{\mathrm{B\,or\,N}} - mE_{\mathrm{Si}} - E_{\mathrm{p}} \quad (3)$$

where E_{d} is the calculated total energy of BNNT containing defects, $E_{\mathrm{B\ or\ N}}$ is the total energy of host boron or nitrogen atoms removed from the nanotube, E_{Si} is the total energy calculated for the atomic Si, E_{P} stands for the total energy calculated for the pristine BNNT and a, b and m are the number of B, N and Si atoms, respectively. The band gap is obtained from the difference between the orbital energies of the LUMO (conduction band minimum) and the HOMO (valence band maximum). To plot the density of states (DOS), we used the Multiwfn software [54].

Global reactivity descriptors measure the overall reactivity of a molecule. Some of descriptors are chemical potential, chemical hardness, global softness, etc. Chemical potential plays an especial important role in semiconductor physics [55]. The DFT-based reactivity descriptors are good prediction tools for studying reactivity especially in probing the regiochemistry of different types of chemical reactions [56–58].

The relation of chemical potential (μ) and the electronegativity (χ) [59, 60] can be written as follows:

$$\mu = -\chi = -\frac{1}{2}(I + A) \quad (4)$$

The global chemical hardness (η) is defined [61] as:

$$\eta = \frac{1}{2}(I - A) \quad (5)$$

where I and A are the first ionization energy and electron affinity, respectively. The chemical meaning of the word "hardness" is the resistance of the chemical potential to change in the number of electrons.

In the finite difference approximation, the ionization energy and electron affinity can be replaced by the E_{HOMO} and E_{LUMO}, respectively:

$$\mu = -\chi = \frac{1}{2}(E_{\mathrm{HUMO}} + E_{\mathrm{LUMO}}) \quad (6)$$

$$\eta = \frac{1}{2}(E_{\mathrm{LUMO}} - E_{\mathrm{HOMO}}). \quad (7)$$

The electrophilicity index (ω) [62], which measures the capacity of an electrophile to accept the maximal number of electrons in a neighboring reservoir of electron sea, is defined according to the following equation

$$\omega = \frac{\mu^2}{2\eta.} \quad (8)$$

The chemical softness (S) is defined as following equation

$$S = \frac{1}{\eta}.$$

NO adsorption on strained and unstrained Si-doped SW-BNNT is explored at M05-2X/6–31+G(d) level of theory. In addition, dispersion-corrected AEs at M05-2X-D3/6–31++G(d,p)//M05-2X/6–31+G(d) level of theory were also calculated in order to find the effect of dispersion and improved basis set on the interaction energy between NO- and Si-doped BNNT.

Results and discussions

Geometric and energetic descriptions of Si-doped (6,0) SW defective BNNTs

As shown in Fig. 1a, there are two unfavorable homonuclear B–B and N–N bonds in a SW defect

region that are connected by B–N bond. In the $\mathbf{Si_B}$, $\mathbf{Si_N}$ and $\mathbf{Si_{N,B}}$ structures, B atom, N atom and both N and B atoms of this bond were replaced with a Si atom, respectively. As shown in Fig. 1, when the SW defect is created, three types of B–N bonds can be found: longitudinal B–N bonds; parallel to the longitudinal direction of the tube that are designed as L_1–L_6, zigzag (diagonal) B–N bonds that are labeled as L_7–L_{18} and one B–N bond orthogonal to the tube axis that is designed as L_{19} (bond connecting the two pentagons and two heptagons in 5–7–7–5 ring fusion).

The experimental studies on the Si-doped multi-walled BNNTs have revealed the formation of Si–B and Si–N bonds in the lattice [63, 64]. In the $\mathbf{Si_B}$- and $\mathbf{Si_N}$-doped SW–BNNTs, one B and N atoms of the vertical B–N bond in the SW defect region was substituted by one Si atom. After structural optimizations, we found that Si doping causes significantly large distortion in defect region. The bond length values of L_1–L_{19} bonds and selected bond angles around the substituted atoms are listed in Table 1. The length of Si–N (L_{16}), Si–B (L_{15}) and Si–B (L_{19}) sp^3-like bonds in $\mathbf{Si_N}$ nanotube (NT) is 1.792, 2.023 and 1.975 Å and that of Si–N (L_{17}), Si–B (L_{18}) and Si–N (L_{19}) bonds in $\mathbf{Si_B}$ nanotube is 1.779, 2.028 and 1.784 Å, respectively, which are much larger than the N–N (L_{16}; 1.449 Å), B–B (L_{18}; 1.713 Å) and B–N (L_{19}; 1.434 Å) sp^2 bonds in un-doped SW-BNNT. The vertical L_{19} bond length is 1.434 Å, 1.975 and 1.784 Å in the SW–BNNT, $\mathbf{Si_N}$ and $\mathbf{Si_B}$ nanotubes, respectively, indicating that vertical B–N bond in un-doped nanotube is shorter than vertical Si–B and Si–N bonds in Si-doped ones. Therefore, substitution of Si atom increases L_{19} bond in both models, so that this increase for $\mathbf{Si_N}$ is greater than $\mathbf{Si_B}$. Since the atomic radius of Si atom is larger than N and B atoms, substitution of N and B by Si in the vertical L_{19} bond increases its bond length. The two other bond lengths between Si and neighboring atoms (L_{16} and L_{15} in $\mathbf{Si_N}$ and L_{17} and L_{18} in $\mathbf{Si_B}$) are longer than those found in SW–BNNT.

In $\mathbf{Si_{N,B}}$ NT, both N and B atoms in L_{19} bond are replaced with two Si atoms. The calculated L_{15}–L_{19} bond lengths in $\mathbf{Si_{N,B}}$ NT are 2.019, 1.751, 1.876, 2.138 and 2.245 Å, respectively. Since the size of Si atom is greater than B and N atoms, optimized L_{19} bond length at the 7–7 ring fusion of the $\mathbf{Si_{N,B}}$ (2.245 Å) is greater than those of $\mathbf{Si_B}$ (1.784 Å), $\mathbf{Si_N}$ (1.975 Å) and un-doped NT (1.434 Å). Therefore, L_{19} bond in $\mathbf{Si_{B,N}}$ NT is weaker than that of $\mathbf{Si_N}$ and $\mathbf{Si_B}$ NTs. Two other bonds (L_{15} and L_{16} in $\mathbf{Si_N}$) and (L_{17} and L_{18} in $\mathbf{Si_B}$) are, respectively, longer and shorter than those of corresponding bonds in $\mathbf{Si_{N,B}}$ NT.

In addition, bond angles around the Si atom in Si-doped NT change with respect to un-doped one. The sum of three angles around the N and B atoms involved in vertical B–N bond in un-doped nanotube

Table 1 Selected bond lengths (Å) and bond angles calculated at M05-2X/6–31+G(d) level for Si-doped SW-BNNTs

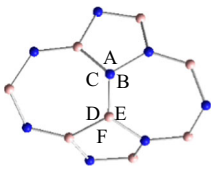

	Bond length						
	L_{15}	L_{16}	L_{17}	L_{18}	L_{19}	$\langle L_{15}+L_{16}+L_{19}\rangle$	$\langle L_{17}+L_{18}+L_{19}\rangle$
Un-doped	1.492	1.449	1.466	1.713	1.434	1.458	1.537
$\mathbf{Si_B}$	1.470	1.444	1.779	2.028	1.784	1.566	1.864
$\mathbf{Si_N}$	2.023	1.792	1.440	1.740	1.975	1.930	1.719
$\mathbf{Si_{N,B}}$	2.019	1.751	1.876	2.138	2.245	2.005	2.086

	Bond angle									
	A	B	C	D	E	F	A + B + C	D + E + F	⟨A + B + C⟩	⟨D + E + F⟩
Un-doped	106.9	118.1	116.4	122.6	124.0	105.5	341.4	352.2	113.8	117.4
$\mathbf{Si_B}$	108.1	119.5	124.7	100.0	105.3	91.1	352.3	296.3	117.4	98.8
$\mathbf{Si_N}$	91.5	103.3	99.9	118.4	122.4	107.1	294.7	347.9	98.2	98.2
$\mathbf{Si_{N,B}}$	93.0	121.6	132.9	73.1	87.3	86.9	347.6	247.4	115.9	82.5

is 341.4° (average bond angle of 113.8°) and 352.2° (average bond angles of 117.4°), respectively, indicating that the N atom is out of tube surface with respect to B atom. When that Si → (B or N) substitution happens, sum of the three angles around the Si atom in **Si$_B$** and **Si$_N$** decreases to 294.7° and 296.3°, respectively, which are smaller than sum of the normal pyramidal angles. Therefore, Si atom in **Si$_N$** and **Si$_B$** NTs preserves pyramidal-like electronic geometry sp^3 with the average bond angles of 98.2° and 98.8°. The increase in bond lengths and a decrease in bond angles around the Si atom forces the Si atom to protrude outwardly from the tube surface (see front view of Fig. 1).

Comparison of the bond angles in **Si$_{N,B}$** NT shows that the sum of three bond angles around the Si atom of the Si → N substitution (347.6°) is greater than that of Si → B substitution (247.4°). In other words, average bond angle around the Si atom of the Si → N substitution (115.9°) is greater than that of Si → B substitution (82.5°). Therefore, it is expected that the distance of Si atom in **Si$_{N,B}$** NT from the surface of NT in Si → B substitution to be greater than that of Si → N substitution, as can be seen in Fig. 1. The average bond angle values around the Si atoms in **Si$_{N,B}$** NT (115.9° and 82.5°) are greater/smaller than those of estimated for **Si$_N$** (98.2°)/**Si$_B$** (98.8°). The calculated E angle of **Si$_B$** NT (105.3°) that almost is consistent with the previous reports [41, 65].

In pristine BNNTs, N atoms and their nearest three B atoms form local pyramid structures. They are not located on the same cylindrical surface so that outer and inner shells occupy by the N and B atoms, respectively [7, 32, 66]. Thus, the radial geometry of the tubular structure is characterized by two concentric cylindrical tubes: all of B atoms forming the inner cylinders and all of the N atoms forming the outer cylinders. The radial buckling (β) is defined [41] by

$$\beta = r_N - r_B$$

where r_B and r_N represent the radii of the B and N cylinders. If the value of β approaches zero, the B and N atoms will be located on the cylindrical surface of the BNNT, while a positive value indicates that the BNNT consists of two cylindrical surfaces with N atoms situated on the outer surface. In (6,0) SW-defected BNNT and Si-doped SW-defected BNNTs, we have defined three types of β at the different areas of Si-doped SW defective BNNTs as shown in Fig. 2. The average value of β for **Si$_B$**, **Si$_N$** and **Si$_{N,B}$** is 0.096, 0.088 and 0.084 Å, respectively, indicating that difference in radii of the outer and inner cylinders in **Si$_B$** is greater than others and in **Si$_{N,B}$** is the smallest value.

The calculated BE and defect formation energies (E_{form}) for SW and Si-doped SW defective BNNTs are reported in Table 2. As can be seen, the BE values for Si-doped SW defective BNNTs **Si$_B$** (7.11 eV), **Si$_N$** (7.08 eV) and **Si$_{N,B}$** (7.07 eV) NTs are smaller than that of BE of SW–BNNT (7.14 eV).

The calculated defect formation energies (E_{form}) of **Si$_B$**, **Si$_N$** and **Si$_{N,B}$** NTs are 4.96, 6.95 and 7.59 eV, respectively, indicating a greater probability for the Si atom to replace the boron atom than the nitrogen atom. As can be seen, the formation energy for **Si$_{N,B}$** NT is greater than **Si$_B$** and **Si$_N$** ones. Therefore, substitution of vertical B–N bond in the SW defect region by Si–Si bond leads to a nanostructure that is less stable than two others. There is a correlation between L_{19} bond length in **Si$_B$**, **Si$_N$** and **Si$_{N,B}$** **NTs**

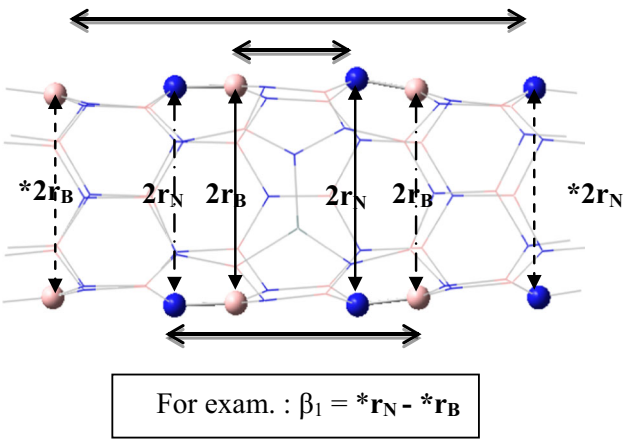

Figure 2 Three defined radial buckling (β) in NTs.

Table 2 Average radial buckling (β), binding energy (BE), defect formation energy (E_{form}), HOMO (E_H), LUMO (E_L) and band gap (E_{L-H}) energies for **NTs** calculated using M05-2X method

	SW-BNNT	Si_B	Si_N	$Si_{N,B}$
β (Å)	0.108	0.096	0.088	0.084
BE (eV)	7.14	7.11	7.08	7.07
E_{form} (eV)	3.07	4.96	6.95	7.59
E_{HOMO} (eV)	−8.05	−6.79	−6.72	−6.95
E_{LUMO} (eV)	−1.23	−1.22	−1.28	−2.11
E_{L-H} (eV)	6.82	5.57	5.43	4.85

and their E_{form}; defect formation energy increases from **Si_B** to **Si_N** and **$Si_{N,B}$ NTs** as the L_{19} bond length increases.

The energies of the highest occupied molecular orbital (E_{HOMO}), the lowest unoccupied molecular orbital (E_{LUMO}) and the energy gap between LUMO and HOMO are tabulated in Table 2. The **$Si_{N,B}$** NT has the lowest value of E_{HOMO} and E_{LUMO} compared to the other two NTs. The energy gap for **$Si_{N,B}$** NT (4.85 eV) is smaller than **Si_N** (5.43 eV) **Si_B** (5.57 eV) and un-doped SW-BNNT (6.82 eV). Therefore, order of energy gap is SW-BNNT > **Si_B** > **Si_N** > **$Si_{N,B}$**. The smallest value of the energy gap in **$Si_{N,B}$** NT can be attributed to smaller value of LUMO energy in **$Si_{N,B}$** (−2.11 eV) compared with others. From a comparison of energy gaps, it can be concluded that the conductivity of **$Si_{N,B}$** NT is the greater and excitation energy of **$Si_{N,B}$** NT is smaller than other two NTs.

Isodensity surfaces of HOMO and LUMO for SW–BNNT, **Si_B**, **Si_N** and **$Si_{N,B}$** NTs are given in Fig. 3. As can be seen, electron density of the HOMO of SW-BNNT is localized on the B–N bonds at the defected area and slightly on the nitrogen atoms in the vicinity of the defected region, but the electron density of HOMO of **Si_B** model mainly localized on the Si atom. Also electron density of LUMO of both SW-BNNT and B–Si model is distributed on the B–N pairs along the tube axis and mainly on the end of the B-terminal. Thus, it is expected that electrophilic sites of SW–BNNT and B–Si models are distributed on the B–N pairs at the end of B-terminated and their nucleophilic site is distributed on the Si atom in the center of defect region. The isodensity surface of the HOMO of **$Si_{B,N}$** NT is almost similar to HOMO of **Si_B** model and its distribution is concentrated on Si atom of the vertical bond in the SW defect region. Also, the isodensity surfaces of the LUMOs of **$Si_{N,B}$** NT have similar behavior for the isodensity surface of the LUMOs of **Si_B** NT. The isodensity surface of the HOMOs of **Si_N** NT is different from that of **Si_B** model so that it is localized on B–B, two Si–B bonds of the SW defect region.

The values of global indices and electric dipole moment for SW defective BNNT and Si-doped SW defective BNNTs before are tabulated in Table 3. One can see that the value of chemical potential, μ, in $Si_{B,N}$ model (−4.88 eV) is smaller than that of SW defective BNNT (−4.01 eV), **Si_B** (−4.00 eV) and **Si_N** (−4.53 eV) models. Decrease in μ upon Si → N substitution in **Si_N** is greater than Si → B substitution in **Si_B**. In Table 3, the **$Si_{N,B}$** model has the minimum value of chemical hardness, η, and maximum values of chemical softness, S, as well as electrophilicity index, ω, compared with the other Si-doped SW defective BNNTs. The dipole moment of **$Si_{N,B}$** model is smaller than **Si_B** and **Si_N** NTs. There is a correlation between η and HOMO–LUMO gap; its value decreases as the HOMO–LUMO gap decreases. Therefore, reactivity of **$Si_{N,B}$** is greater than others.

Densities of states (DOSs) can be used as a valuable tool for analyzing the nature of electronic structure. Si atom has the different number of valence electrons than the atoms of the B and N. Accordingly, when a B (or N) atom is substituted by a Si atom, the extra valence electron (or hole) makes available defect levels within the HOMO–LUMO gap of SW-BNNT. Total and partial DOSs of **Si_B**, **Si_N** and **$Si_{N,B}$** NTs are shown in Fig. 4. As can be seen, the band gaps of Si-doped SW-BNNTs depend on the positions where the Si atom is substituted. As we know, all electrons in a hexagonal structure of SW-BNNT **$Si_{N,B}$ NT** are paired and the structure should not present spin polarization while the presence of a Si atom in **Si_B** and **Si_N** NTs causes a net spin polarization. In fact, the unpaired electron in the **Si_B** and **Si_N** NTs induces a magnetic moment.

Because of the presence of Si atom, DOS curves of **Si_B**, **Si_N** and **$Si_{N,B}$** NTs show impurity states in HOMO–LUMO gap. It is clear that the Si impurity has a significant contribution to the DOS appeared in the band gap, so Si doping of BNNT improves the electronic transport property of the SW-BNNT. Compared with SW-BNNT, Fermi level in **Si_B**, **Si_N** and **$Si_{N,B}$** NTs moves toward greater energy. As can be seen, Si doping in Si_B causes that the new donor-like impurity state to be appear near the conduction band edge and at the same time the new peak appears on the top of the valence band compared with the SW-BNNT, indicating that the Si_B NT is an n-type semiconductor with donor impurity states, in good agreement with results found for Si_B-BNNT system [27, 67]. While for the electron poor **Si_N** NT, only a new local energy level appears on the top of the valence band, which indicates that Si doping in **Si_N** leads to creating an electronic hole and, in turn, increase in the conductivity of the BNNT. This fact implies that the **Si_N** NT is a typical *p*-type semiconductor. In **$Si_{N,B}$**, two new states are separated by about 4.85 eV.

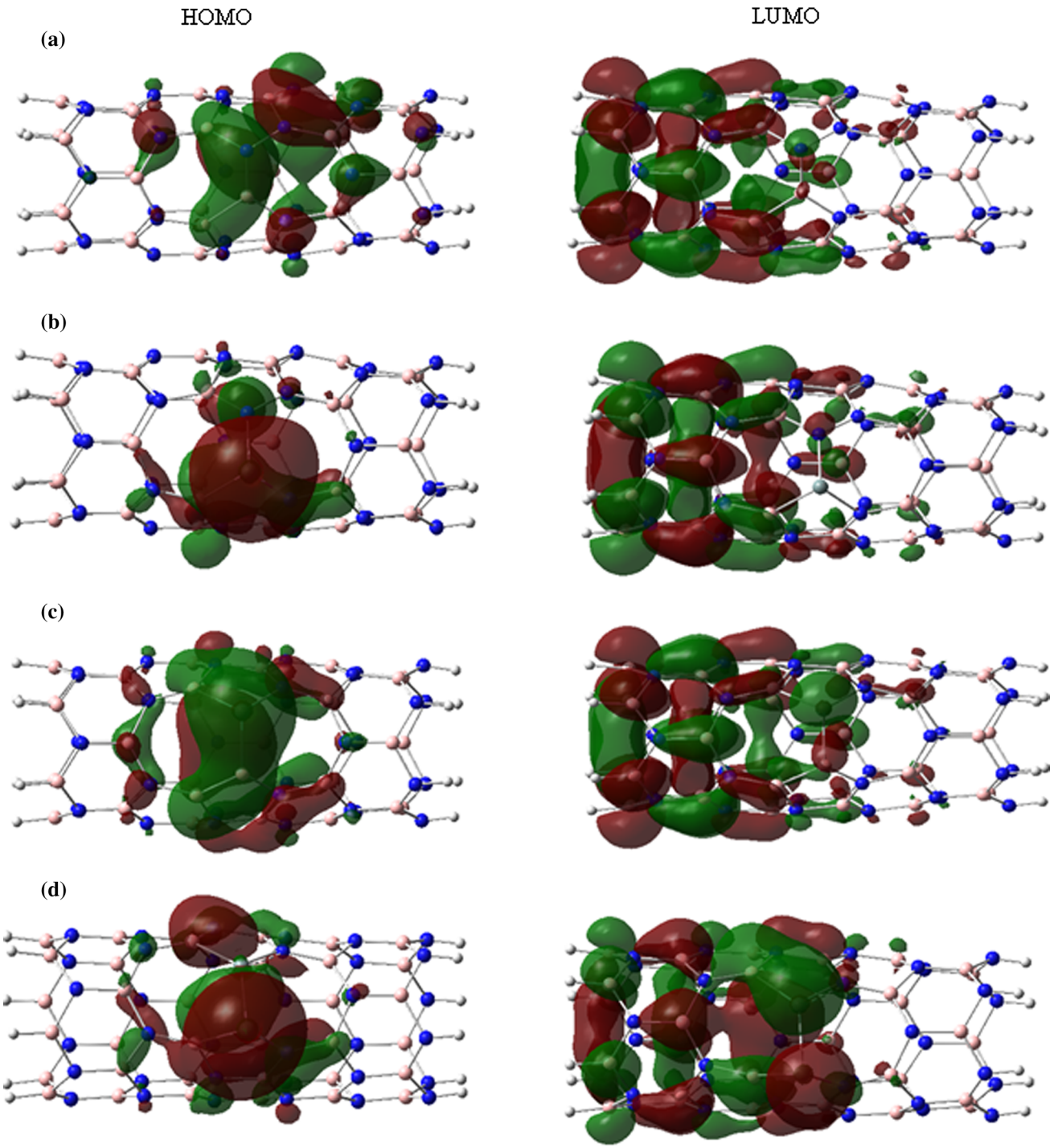

Figure 3 Isodensity surfaces of HOMO (*left side*) and LUMO (*right side*) for **a** SW-BNNT, **b** $\mathbf{Si_B}$, **c** $\mathbf{Si_N}$ and **d** $\mathbf{Si_{N.B}}$ at the isovalue of 0.02 au. The N, B and Si atoms are represented by *blue*, *pink* and *gray spheres*.

Effect of axial strain on the geometric and energetic properties of Si-doped (6,0) SW defective BNNTs

The geometric and energetic properties of Si-doped SW defective BNNTs can be affected by axial strain. The change in structural parameters of mentioned NTs upon axial strain is given in Fig. 5. In addition, schematic representation of percentage change in bond lengths upon axial strain is given in Fig. 6. During the axial strain process in $\mathbf{Si_B}$ model, $L_{8–13}$ bonds are stretched up to 5%, L_1, L_3 and L_5 as well as

Table 3 Values of L–H gap, electronic chemical potential (μ), hardness (η), softness (S), electrophilicity index (ω), and dipole moment (Q) for **D**–**N** models

	L–H (eV)	μ (eV)	η (eV)	ω (eV)	S (eV^{-1})	Q (Debye)
BNNT	7.17	−4.64	3.58	3.32	0.28	6.23
SW-BNNT	6.82	−4.01	3.41	3.16	0.29	5.88
Si_B	5.57	−4.00	2.78	2.88	0.36	5.58
Si_N	5.43	−4.53	2.72	2.95	0.37	6.23
$Si_{N,B}$	4.85	−4.88	2.42	4.23	0.41	5.56

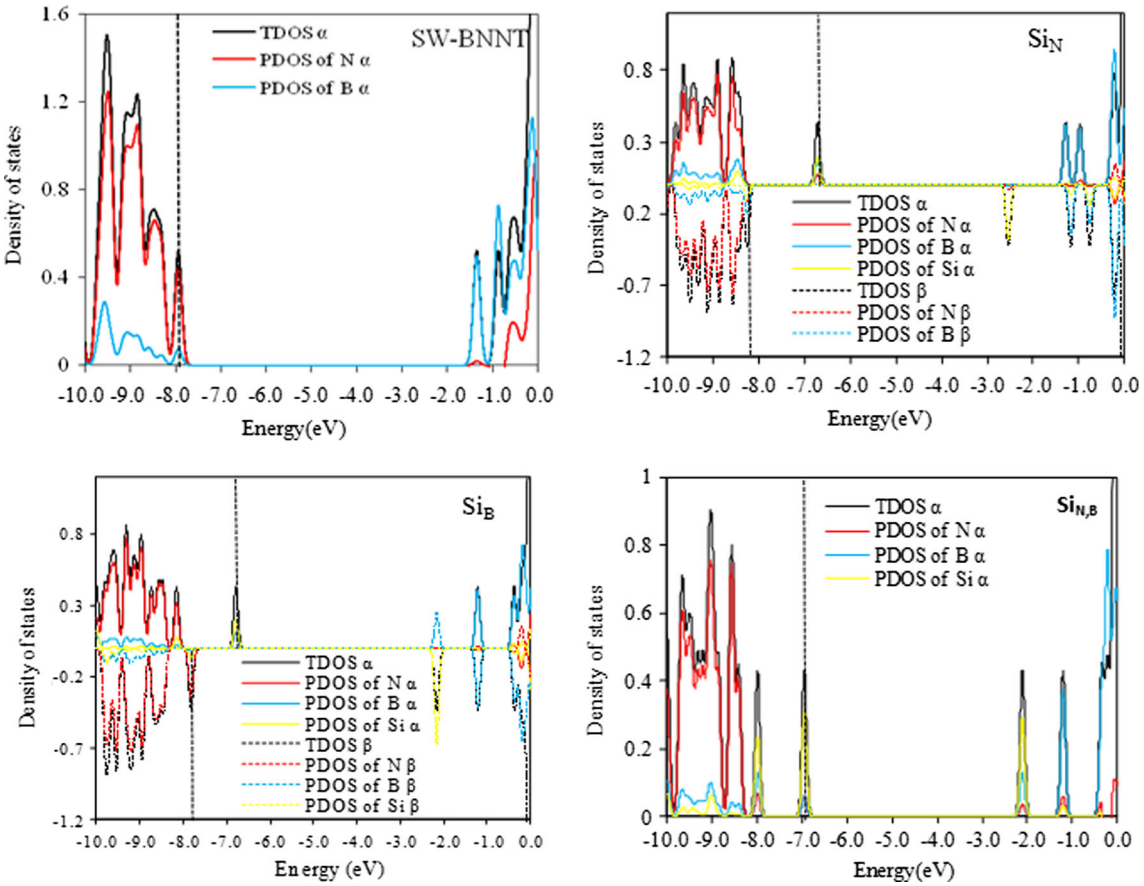

Figure 4 Density of states (DOS) of SW-BNNT, $\mathbf{Si_N}$, $\mathbf{Si_B}$ and $\mathbf{Si_{N,B}}$ models. *Black curves* indicate the total DOS, whereas *red*, *blue*, and *yellow curves* indicate N, B and Si partial DOSs, respectively. *Black vertical dashed lines* mark the Fermi levels.

L_{15}–L_{18} bonds are elongated up to 10% and L_2, L_4 and L_6 bonds are lengthened up to 25%. The L_7, L_{14} and L_{19} bonds decrease under axial strain. The elongation of L_6 bond is greatest, and L_{10} bond is smallest in $\mathbf{Si_B}$.

Under the axial strain in $\mathbf{Si_N}$ NT, $L_{7–10}$ and $L_{12–14}$ as well as L_{17} bonds are lengthened up to 5%, $L_{1–L6}$ and $L_{15–}L_{16}$ as well as L_{18} bonds are stretched up to 15% and L_{11} and L_{19} bonds is shortened; so that the greatest and smallest stretching is related to L_5 and L_{10}, respectively. The vertical L_{19} bond at the 7–7 ring fusion is decreased under axial strain.

In $\mathbf{Si_N}$ and $\mathbf{Si_B}$ NTs, the rapid change in bond lengths was not observed, but the changes in L_{18} bond length in $\mathbf{Si_{N,B}}$ are suddenly so that percent of the changes observed for this bond is 56% under strain employed. The L_{10}–L_{15} are lengthened up to 5%, L_2, L_3, L_5, L_6, L_8 and L_{19} bonds are stretched up to 10%, L_1 and L_4 as well as L_{16} bonds are elongated up to 25%, and L_7, L_9 and L_{17} bonds is shortened upon the vertical strain. In contrast to that seen for vertical L_{19} bond localized between two 7–7 rings in $\mathbf{Si_N}$ and $\mathbf{Si_B}$, this bond in $\mathbf{Si_{N,B}}$ is lengthened upon the strain.

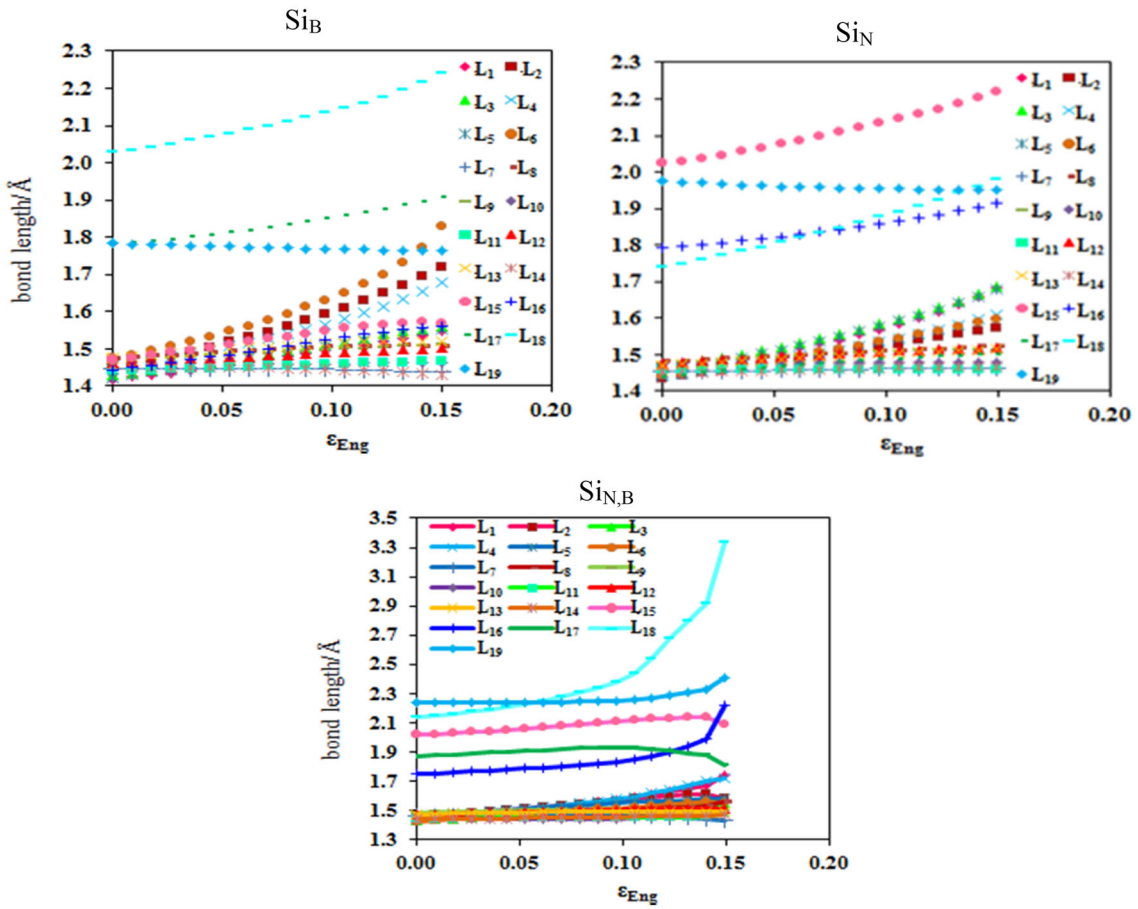

Figure 5 Change in L_1–L_{19} bond lengths upon axial strain in $\mathbf{Si_N}$, $\mathbf{Si_B}$ and $\mathbf{Si_{N,B}}$ NTs.

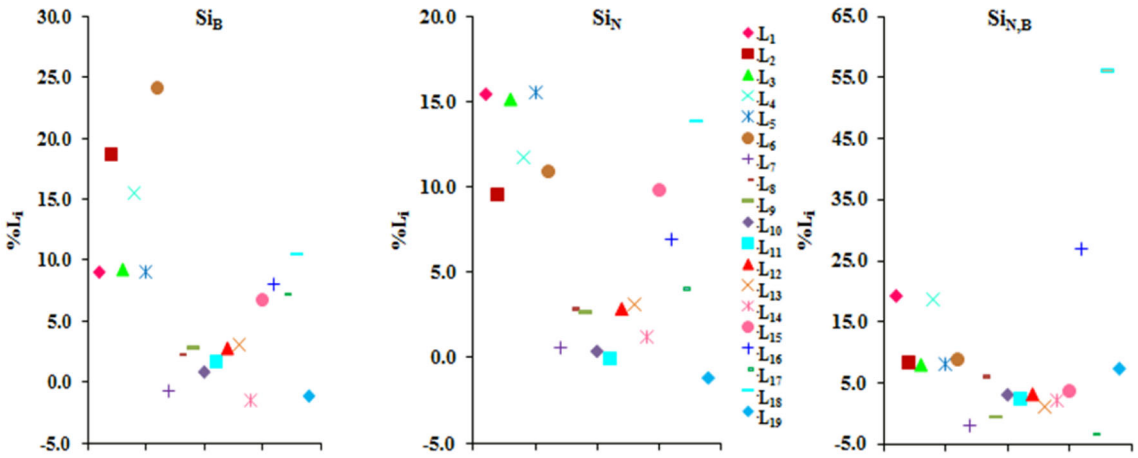

Figure 6 Percent of change in L_1–L_{19} bind lengths in $\mathbf{Si_N}$, $\mathbf{Si_B}$ and $\mathbf{Si_{N,B}}$ NTs upon axial strain.

In addition, the most sensitive NT against axial strain is $\mathbf{Si_{N,B}}$ model. The predicted fracture progression in $\mathbf{Si_N}$, $\mathbf{Si_B}$ and $\mathbf{Si_{N,B}}$ NTs versus axial strain is shown in Fig. 7.

The change in the sum of three bond angles around the N (A, B and C) and B (D, E and F) atoms of vertical L_{19} bond in un-doped SW and corresponding atoms in Si-doped NTs $\mathbf{Si_N}$, $\mathbf{Si_B}$ and $\mathbf{Si_{N,B}}$ is given in Fig. 8. As can be seen, *A* and *F* angles during the axial strain increase and *B*, *C*, *D* and *E* angles decrease in both $\mathbf{Si_N}$ and $\mathbf{Si_B}$ NTs. The average value of the *A*, *B* and *C* decreases and that of *D*, *E* and *F* increases

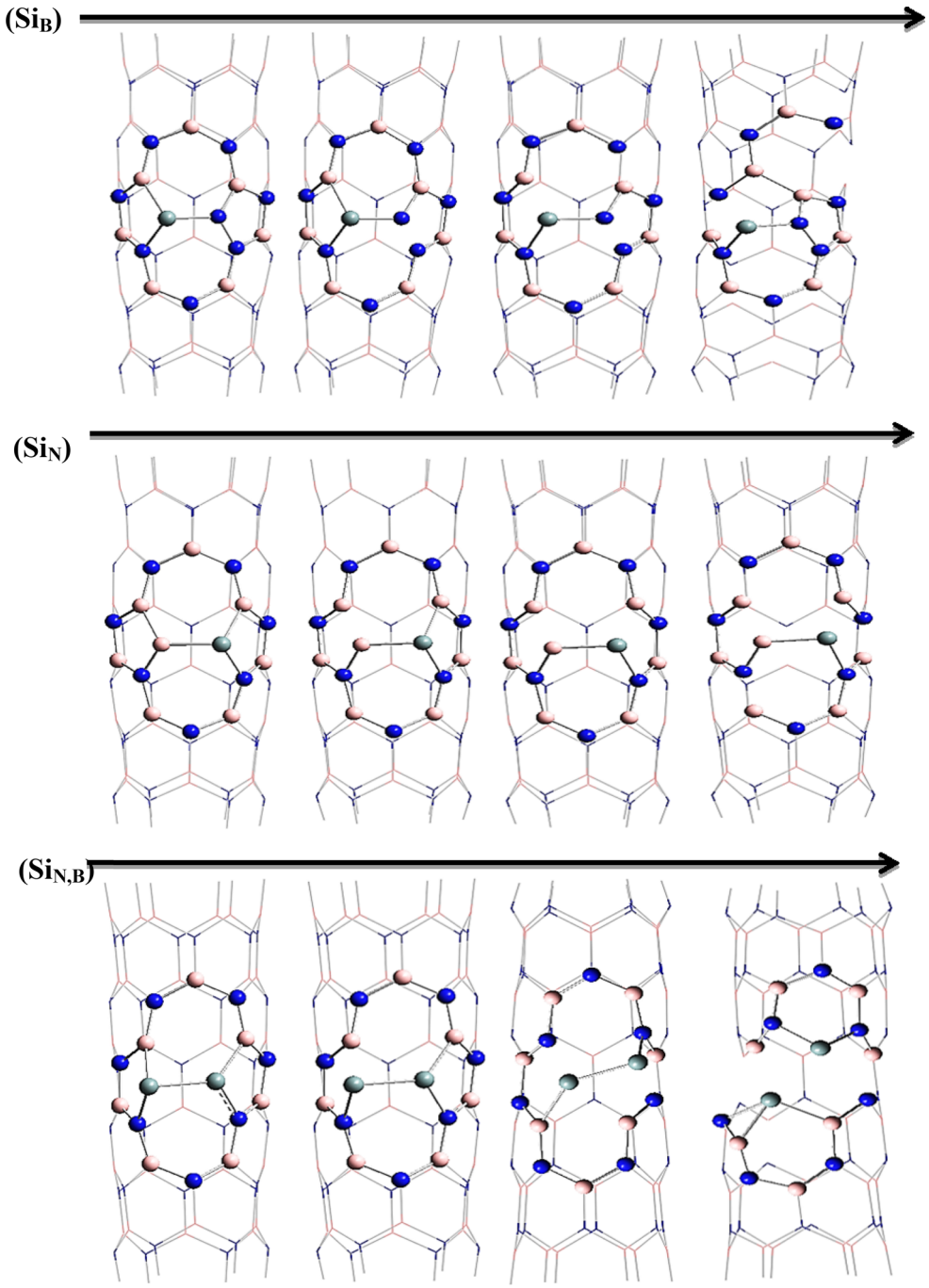

Figure 7 Predicted fracture progression in $\mathbf{Si_N}$, $\mathbf{Si_B}$ and $\mathbf{Si_{N,B}}$ NTs versus axial strain. The B, N and Si atoms are represented in *pink*, *blue* and *silver*, respectively.

upon axial strain in both NTs. The situation in $\mathbf{Si_{N,B}}$ is different. In this NT, *C* and *A* angles increase, *D* and *B* ones decrease and *E* as well as *F* angles do not change nearly upon employing strain. The average value of the *A*, *B* and *C* angles at first decreases and then increases in $\mathbf{Si_{N,B}}$.

The change of radial buckling (β) upon axial strain is given in Fig. 9. This figure shows that the mean values of β for all three doped NTs are positive during the applied axial strain, indicating that the N atoms sit on the outer surface. However, the difference in the radii of the B and N cylinders (β value) of the $\mathbf{Si_B}$ model first decreases and then increases upon elongation of the NT.

The change in the BE and formation energies of Si-doped $\mathbf{Si_N}$, $\mathbf{Si_B}$ and $\mathbf{Si_{N,B}}$ NTs are given in Fig. 10. As can be seen, the BE value slightly decreases and formation energy increases when the NTs are stretched.

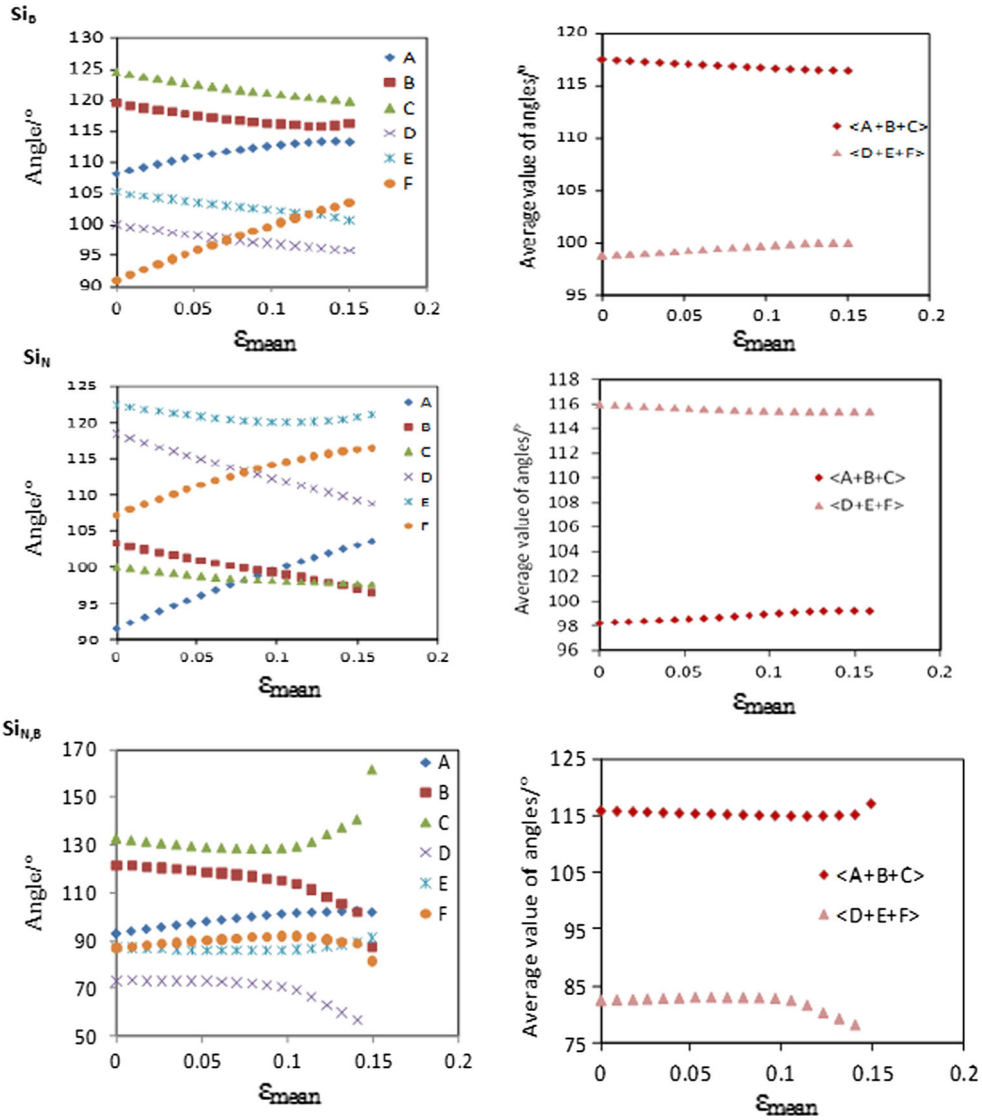

Figure 8 Changes in A–F angles upon axial strain in Si_N, Si_B and Si_{NB} NTs (*left*). Variation of the average value of angles versus axial strain (*right*).

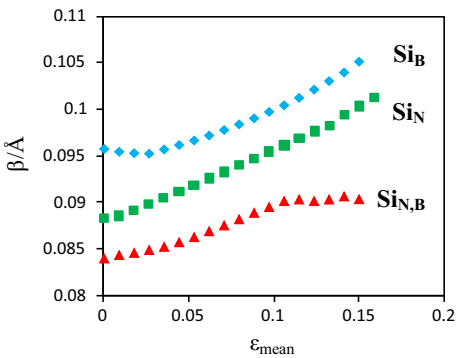

Figure 9 Change in average value of radial buckling (β) under axial strain.

The exceptional resistance of nanotubes to failure is ultimately due to the inherent strength of the constituent chemical bonds and their nearly perfect organization over the microns of the length of the rolled graphite sheet [33]. The elastic strain engineering is one of the nonchemical tools for tuning the electronic properties of nano materials. As expected, since NTs are stretched during axial strain, it is clear that the BE of NTs decreases. Nevertheless, based on the type of NT, their failure is predicted to occur at significantly larger mechanical load. Our results (Fig. 10) show that after 15% tensile strain, BE decreases only ~4.5%. Therefore, the stability of NTs slightly decreases upon axial strain applied and this does not mean that the NT is energetically unstable for further applications. We have checked elasticity of NTs by removing limitations employed during axial strain. After elimination of limitations in NTs, strained NTs are converted to unstrained NT.

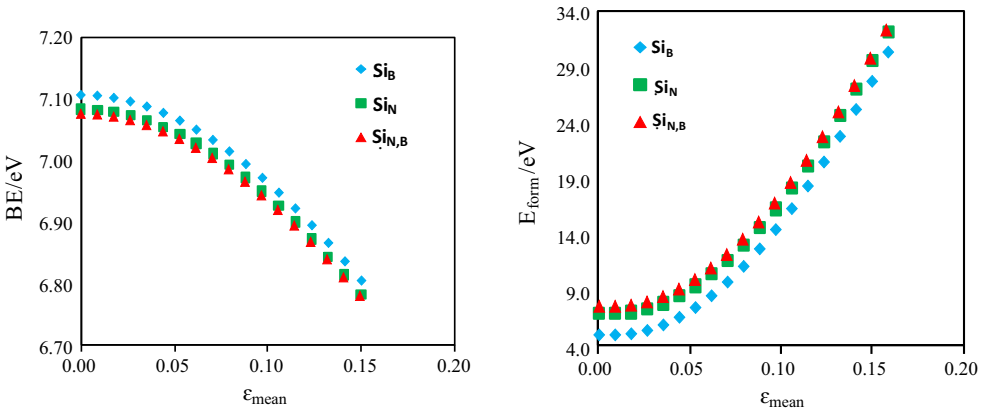

Figure 10 Variations of binding energy (*left*) and defect formation energy (*right*) against ε.

Although stability of stretched NTs is slightly smaller than unstrained ones, they can retain enough their stability; as the strained BNNTs experimentally have been utilized for different applications such as gas storage [68].

The change in E_{HOMO}, E_{LUMO} and $E_{L–H}$ as functions of the axial strain in Si-doped SW defective BNNTs is also plotted in Fig. 11. As can be seen, upon axial strain, the E_{HOMO} of **Si$_N$** and **Si$_B$** models increases, whereas E_{HOMO} of **Si$_{N,B}$** model first increases, then decreases and after that raises again. However, an unlike behavior is observed for E_{LUMO} of models, so that the E_{LUMO} of **Si$_N$** and **Si$_B$** decreases and that of **Si$_{N,B}$** first rises and then decreases. Figure 11c shows that the energy gap ($\Delta E_{L–H}$) of **Si$_N$** and **Si$_B$** models decreases continuity and that of **Si$_{N,B}$** model first smoothly decreases, then suddenly increases and next reduces again. As can be seen, increase in the energy gap of **Si$_{N,B}$** does not reach the initial value of energy gap **Si$_N$** and **Si$_B$** models. Thus, it can be predicted that the conductivity of **Si$_N$** and **Si$_B$** models increases upon the axial strain and for **Si$_{N,B}$** model first increases slowly, then decreases and finally increases.

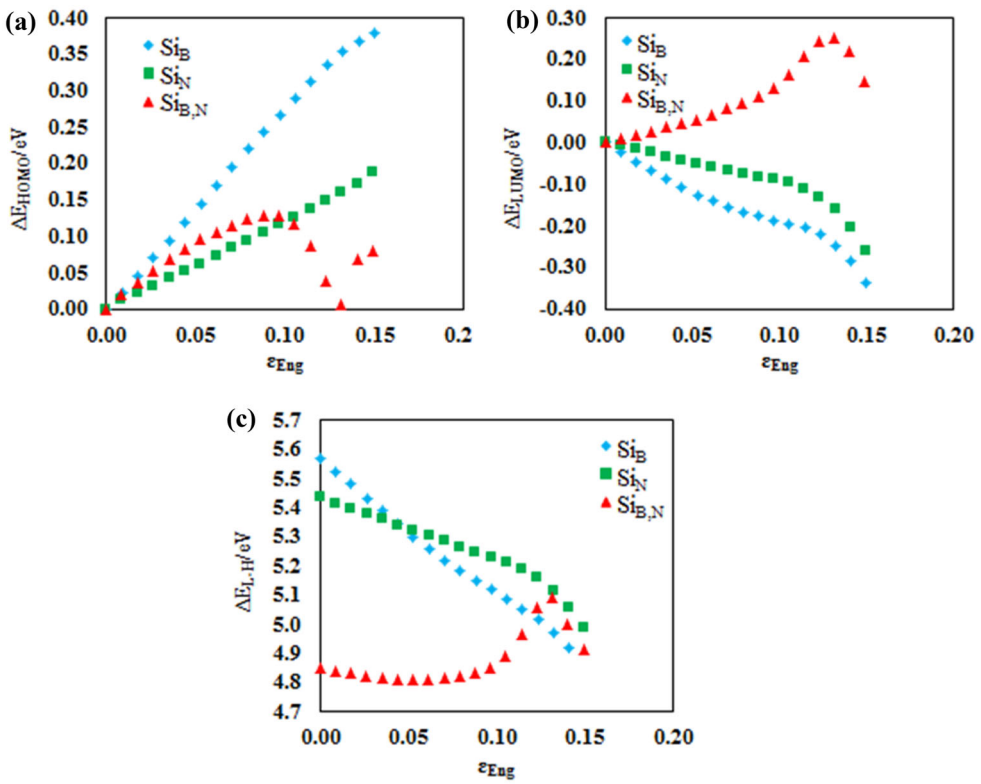

Figure 11 Variations of **a** HOMO energy (ΔE_{HOMO}), **b** LUMO energy (ΔE_{LUMO}) and **c** HOMO–LUMO gap ($\Delta E_{L–H}$) of (6,0) Si-doped SW–BNNTs under axial strain.

Variation of chemical potential ($\Delta\mu$), chemical hardness ($\Delta\eta$), electrophilicity index ($\Delta\omega$), chemical softness (ΔS) and dipole moment (ΔQ) of Si-doped $\mathbf{Si_N}$, $\mathbf{Si_B}$ and $\mathbf{Si_{N,B}}$ NTs upon axial strain are given in Fig. 12. As shown, μ value of all NTs first increases during axial strain up to $\varepsilon \approx 0.11$ and then decreases, in contrast to those of observed for SW defective BNNT [34]. The increase in μ upon axial strain for $\mathbf{Si_{N,B}}$ NT is greater than others. The results show that the chemical hardness for $\mathbf{Si_N}$ and $\mathbf{Si_B}$ decreases while for $\mathbf{Si_{N,B}}$ NT first slowly decreases, then increases and finally decreases, in good agreement with those of observed for electrophilicity index and chemical softness. Therefore, the reactivity behaviors of $\mathbf{Si_N}$, $\mathbf{Si_B}$ upon axial strain are different from that of $\mathbf{Si_{N,B}}$.

The BNNTs have polar structures, and their dipole moments are affected by defect type. The values of dipole moments of SW defective BNNTs, $\mathbf{Si_N}$, $\mathbf{Si_B}$

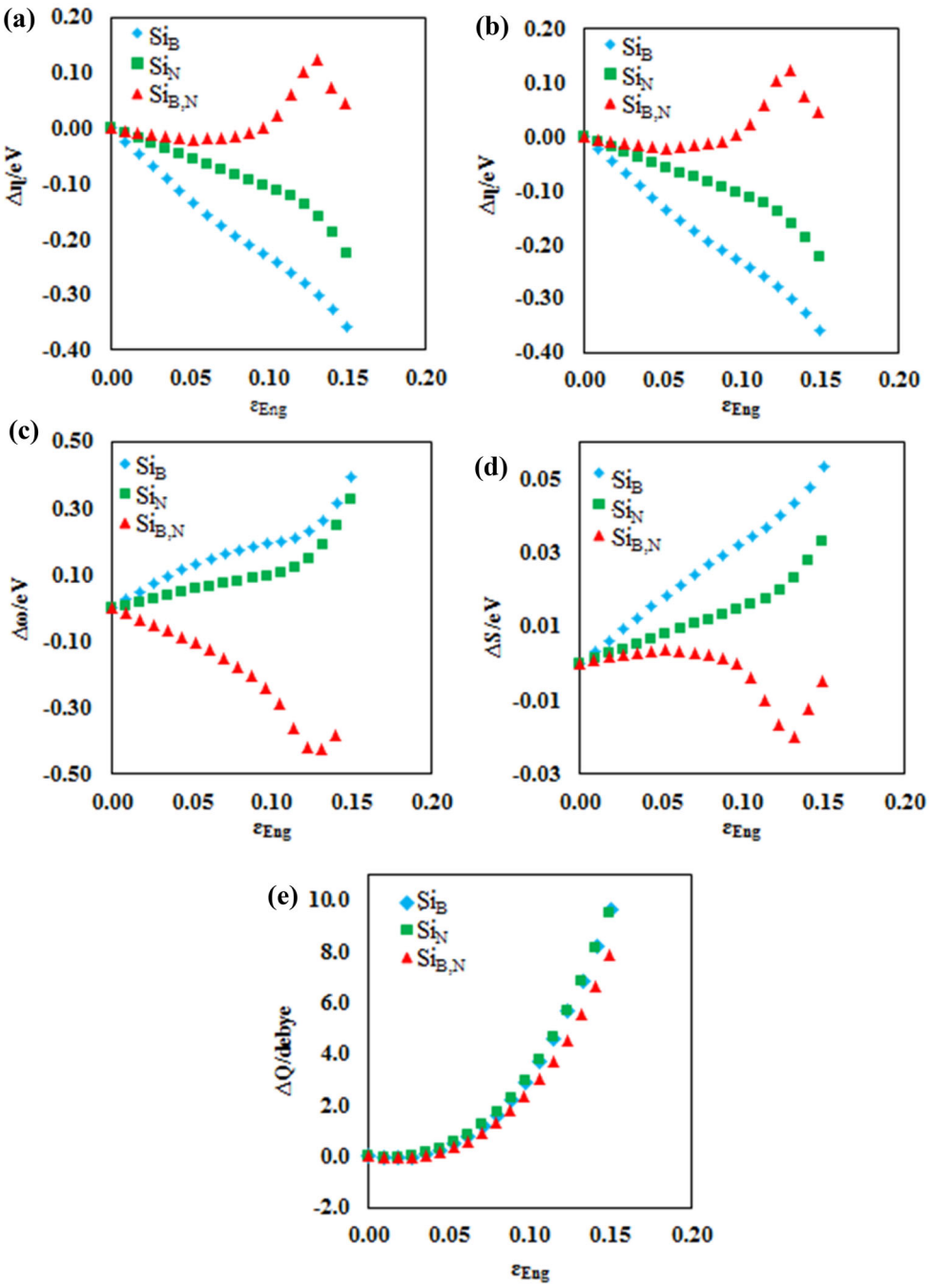

Figure 12 Variations of **a** chemical potential ($\Delta\mu$), **b** chemical hardness ($\Delta\eta$), **c** electrophilicity index ($\Delta\omega$), **d** chemical softness (ΔS) and **e** dipole moment (ΔQ) of (6,0) Si-doped SW defective BNNTs at different strains.

and $\mathbf{Si_{N,B}}$ NTs models are 5.88, 6.23, 5.58 and 5.56, respectively, so the $\mathbf{Si_N}$ model has the most polar structures. The axial strain causes which the values of dipole moments change sharply. From Fig. 12e, it is clear that the dipole moment of NTs increases highly upon the axial strain.

NO adsorption on strained and unstrained Si-doped SW-BNNT

Adsorption on the Si_B and Si_N SW-BNNT

The NO molecule can be adsorbed on strained and unstrained Si_{1-2}-doped SW-BNNTs through either N or O atoms. To explore the stable adsorption configurations of a NO molecule on Si-doped SW-BNNT, the various possible adsorption geometries are considered. Complexes formed from the attachment of NO to unstrained and strained (with 10% strain) Si-doped SW-BNNTs are shown in Fig. 13. The NO molecule has two orientations with respect to the tube axis. The $\mathbf{Si_Z}$-NO and $\mathbf{Si_Z}$-ON symbols represent that the NO molecule is attached to Si by N and O atoms, respectively. For each of the $\mathbf{Si_N}$ and $\mathbf{Si_B}$ NTs interacting with NO gas, complexes of these two types were found on the potential energy surfaces. The electronic adsorption energies (AEs), HOMO, LUMO and band gap energies obtained at M05-2X/6–31+(d) level of theory for $\mathbf{Si_N}$-**NO**, $\mathbf{Si_N}$-**ON**, $\mathbf{Si_B}$-**NO1**, $\mathbf{Si_B}$-**NO2**, $\mathbf{Si_{NB}}$-**NO-1**, $\mathbf{Si_{NB}}$-**ON1-**, $\mathbf{Si_{NB}}$-**NO2** and $\mathbf{Si_{NB}}$-**O-N2** complexes are given in Table 4.

During the geometry optimization, $\mathbf{Si_B}$-**ON** is converted to another $\mathbf{Si_B}$-**NO** with different configuration $\mathbf{Si_B}$-**NO2**. Therefore, two types of structures $\mathbf{Si_B}$-**NO1** and $\mathbf{Si_B}$-**NO2** are predicted for unstrained $\mathbf{Si_B}$-**NO** that direction of NO in the two structures is different. For 1Si-doped SW-BNNTs, AEs calculated for $\mathbf{Si_N}$-**NO**, $\mathbf{Si_N}$-**ON**, $\mathbf{Si_B}$-**NO1** and $\mathbf{Si_B}$-**NO2** complexes with unstrained NTs are −26.42, −1.39, −29.92 and −32.69 kcal mol^{-1}. These results first reveal that adsorption of NO gas on the $\mathbf{Si_B}$ NTs is energetically more favorable than those of $\mathbf{Si_N}$ NTs. In other words, an energetically favored site for adsorption of NO gas in Si-doped SW-BNNTs is above the Si → B site (the Si atom doping into the B site). Second, adsorption is energetically much less favorable for the $\mathbf{Si_N}$-**ON** than $\mathbf{Si_N}$-**NO.** In contrast to what we see in the $\mathbf{Si_{N-}}$, adsorption of NO on the $\mathbf{Si_B}$ from its O head is energetically less favorable than that of its N head. It can be concluded that the energetically most favorable site for NO adsorption arises when the NO is attached to $\mathbf{Si_B}$ from its N head.

Dispersion-corrected AEs at M05-2X-D3/6–31 ++G(d,p)//M05-2X/6–31+G(d) level of theory were also calculated in order to find the effect of dispersion and improved basis set on the interaction energy between NO and Si-doped BNNT. Dispersion-corrected BEs are −27.00, −2.00, −33.43, −33.34 kcal mol^{-1}, respectively. As can be seen, including the dispersion contribution to energies, AEs increase slightly.

AEs obtained for Si-doped–NO complexes are comparable with those reported in the literature. The adsorption energy (∼−16 kcal mol^{-1}) has been reported for the (8,0) SiCNT-NO complex using PBE method [69]. The AEs reported for interaction of NO with C-doped SW-BNNTs at M06-2X/6-31 ++G(d,p) level of theory are −31.29, −9.63, −33.62 and +6.96 kcal mol^{-1}, respectively [24]. As mentioned above, AEs calculated for $\mathbf{Si_N}$-**NO**, $\mathbf{Si_N}$-**ON**, $\mathbf{Si_B}$-**NO1** and $\mathbf{Si_B}$-**NO2** complexes are −26.42, −1.39, −29.92 and −32.69 kcal mol^{-1}, respectively. Therefore, Si_B-doped SW-BNNT shows an increased ability for adsorption of NO, as compared to the C_B-doped SW-BNNT.

The N–O distance in the free NO gas is 1.145 Å and increases to 1.209, 1.267, 1.207 and 1.208 Å in $\mathbf{Si_N}$-**NO,** $\mathbf{Si_N}$-**ON,** $\mathbf{Si_B}$-**NO1** and $\mathbf{Si_B}$-**NO2** complexes, respectively, in good agreement with the order of changes in AEs. The elongation of N–O bond can be attributed to the charge transferred from NT to π* orbital of NO molecule. NBO analysis shows that the charge transfer values are 0.463, 0.571, 0.428 and 0.474 au, respectively, especially for $\mathbf{Si_N}$-**ON** complex with the largest charge transfer of 0.571 au, in good agreement with the order of NO bond distances. Besides, Si–N(O) distance is 1.874, 1.777, 1.866 and 1.866 Å in $\mathbf{Si_N}$-**NO,** $\mathbf{Si_N}$-**ON,** $\mathbf{Si_B}$-**NO1** and $\mathbf{Si_B}$-**NO2** complexes, respectively. There is not a direct correlation between AEs and Si–N(O) distance.

Band gap for $\mathbf{Si_N}$ and $\mathbf{Si_B}$ is 5.43 and 5.50 eV that increases to 5.61, 5.49, 5.81 and 5.96 eV in $\mathbf{Si_N}$-**NO**, $\mathbf{Si_N}$-**ON**, $\mathbf{Si_B}$-**NO1 and** $\mathbf{Si_B}$-**NO2** complexes, respectively. The percentage change in the band gap energy of $\mathbf{Si_N}$-**NO,** $\mathbf{Si_N}$-**ON,** $\mathbf{Si_B}$-**NO1** and $\mathbf{Si_B}$-**NO2** is 3.3, 0.9, 7.0 and 4.3, respectively. On the other hand, the net charge transfer from the electronic-rich Si-doped NT to the NO molecule is 0.428–0.571 au compared to that of 0.22 and 0.15 au reported for $\mathbf{Si_B}$-**ON** and $\mathbf{Si_N}$-**ON** complexes formed from interaction between NO

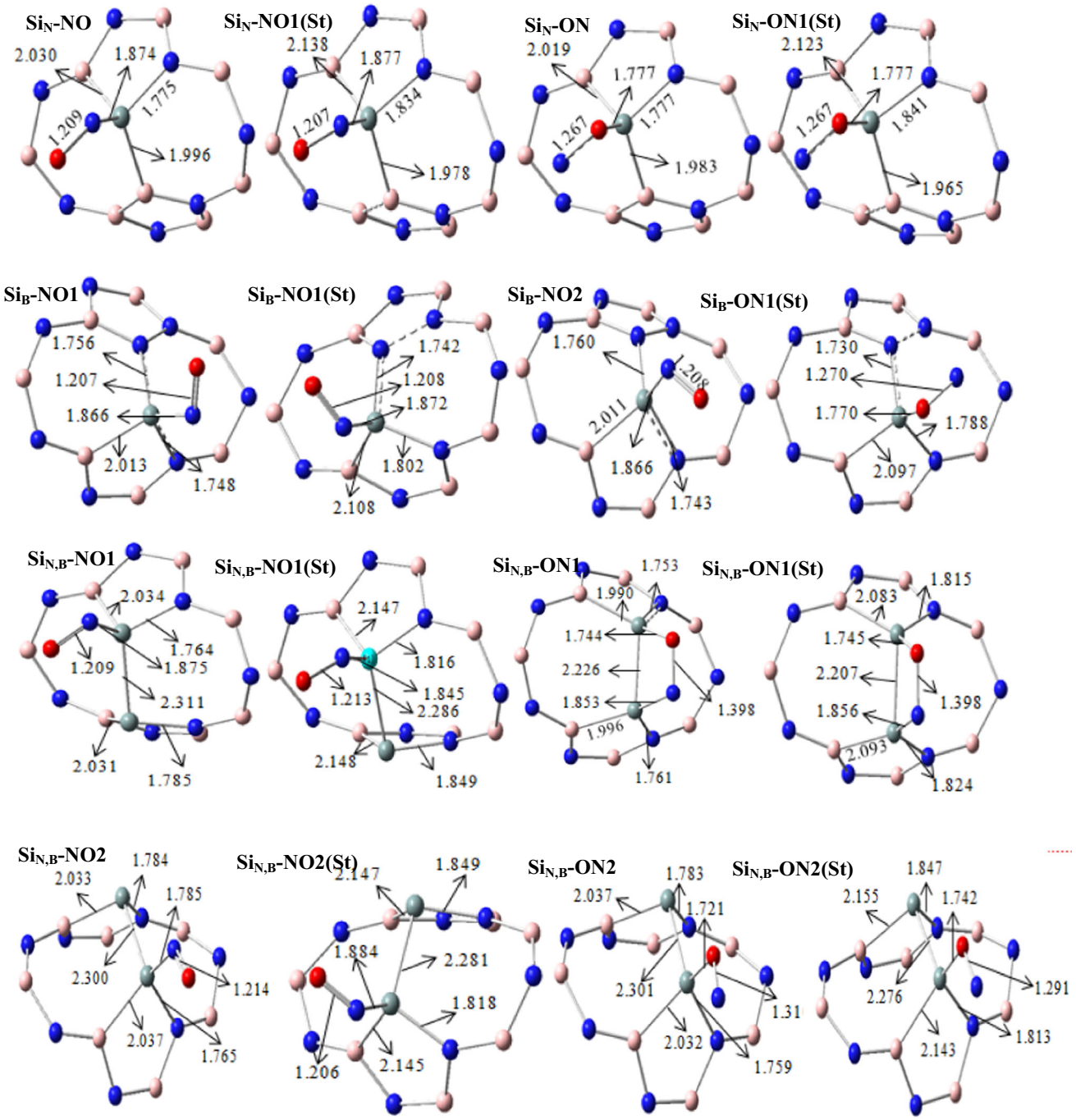

Figure 13 Selected structural parameters of unstrained Si-doped SW-BNNT–NO complexes and 10% strained Si-doped SW-BNNT–NO complexes calculated at ONIOM(M05-2X/6–31+G(d):M05-2X/STO-6G) level. Distances are given in Å.

and Si-doped BNNTs [45]. Therefore, it can be predicted that the Si-doped SW-BNNTs are more sensitive than Si-doped BNNTs toward NO gas. The results indicate that the electronic property of the Si-doped BNNTs changes upon adsorption of the NO molecule, so that these changes for **Si$_B$-NO1** and **Si$_B$-NO2** complexes is greater than those of **Si$_N$-NO** and **Si$_N$-ON** ones, in good agreement with results of the band gap energy. Therefore, the sensitivity of **Si$_B$**-doped NT toward the NO is remarkably greater than that of **Si$_N$** one. It can be concluded that Si-doped NT not only can adsorb the NO molecule strongly, but also may sense its presence because of the change of the tube band gap.

Table 4 Adsorption energies (E_{ads}), HOMO (E_{HOMO}), LUMO (E_{LUMO}) and band gap energies (E_g), the charges on the N and O atoms (q_N, q_O) and the total NBO charge on the NO molecule (CT_{NBO}) of various configurations of Si-doped SW-BNNT–NO complexes

	E_{ads} (kcal mol^{-1})	E_{HOMO} (eV)	E_{LUMO} (eV)	E_g (eV)	q_N (au)	q_O (au)	CT_{NBO} (au)
Si_N-NO[a]	−26.42 (−24.96)	−7.48 (−7.38)	−1.87 (−1.87)	5.61 (5.51)	−0.181 (−0.186)	−0.282 (−0.275)	−0.463 (−0.461)
Si_N-ON[a]	−1.39 (0.83)	−7.39 (−7.31)	−1.90 (−1.90)	5.49 (5.41)	−0.044 (−0.029)	−0.527 (−0.543)	−0.571 (−0.572)
Si_B-NO1[a,b]	−29.92 (−31.72)	−7.61 (−7.50)	−1.79 (−1.6)	5.81 (5.89)	−0.194 (−0.227)	−0.234 (−0.260)	−0.428 (−0.487)
Si_B-NO2[a,c]	−32.69 (−8.65)	−7.62 (−7.16)	−1.66 (−1.40)	5.96 (5.76)	−0.218 (−0.027)	−0.256 (−0.573)	−0.474 (−0.600)
Si_{NB}-NO1[a]	−18.78 (−15.73)	−7.04 (−6.92)	−1.65 (−1.73)	5.39 (5.20)	−0.193 (−0.219)	−0.278 (−0.271)	−0.471 (−0.490)
Si_{NB}-ON1[a]	−33.27 (−27.14)	−7.56 (−7.27)	−1.21 (−1.41)	6.35 (5.86)	−0.366 (−0.370)	−0.669 (−0.674)	−1.035 (−1.044)
Si_{NB}-NO2[a]	−8.75 (−19.37)	−6.99 (−6.94)	−2.03 (−1.42)	4.96 (5.52)	−0.264 (−0.469)	−0.242 (0.273)	−0.506 (−0.196)
Si_{NB}-ON2[a]	10.32 (12.52)	−7.05 (−7.12)	−1.69 (−1.44)	5.36 (5.58)	−0.001 (−0.209)	−0.630 (0.219)	−0.631 (−0.010)

The data in parenthesis correspond to various configurations of NO on Si-doped SW-BNNT after 10% engineering strain (ε_{Eng})

[a] Symbols used in the text for strained complexes having a **St** code after complex name

[b] **Si_B-NO(St)** in strained complex

[c] **Si_B-ON(St)** in strained complex

To gain deeper insights into the electronic structure of the Si-doped SW-BNNTs, we further assessed their density of states (DOS). The presence of a Si atom in **Si_N** and **Si_B** NTs causes the appearance of an unpaired electron and therefore a net spin moment. Therefore, Si doping results in the spin polarization and induces spontaneous magnetization. To explore whether Si doping can induce the spin polarization, the spin DOSs **Si_N**, **Si_B**, **Si_N-NO**, **Si_B-NO** are calculated and shown in Figs. 14 and 15. From this figure, it can be found that new local states are appearing and spin-up and spin-down DOSs are different in the band gap region, indicating that Si doping results in the spin polarization and induces spontaneous magnetization. As can be seen, upon adsorption of NO, Fermi level in these complexes is shifted toward the valence bond and in turn, band gap increases.

To the best of our knowledge, interaction between strained BNNTs and diatomic gases is not reported and is explored firstly in this work. Before treating AEs for strained systems, it should be noted that in contrast to unstrained NT, **Si_B-ON** is a stable complex and is not converted to **Si_B-NO.** In other words, although unstrained **Si_B-ON** is unstable, but strained **Si_B-ON(St)** complex is energetically stable. AEs calculated for **Si_N-NO (St), Si_N-ON(St)**, **Si_B-NO(St)** and **Si_B-ON(St)** complexes after 10% tensile strain at M05-2X/6–31+G(d) level of theory are −24.96, 0.83, −31.72 and −8.65 kcal mol^{-1}, respectively, indicating that AE for **Si_N-NO(St)**, **Si_N-ON(St)** and **Si_B-ON(St)** decreases after 10% tensile strain and that of **Si_B-NO(St)** increases slightly. Decrease in AE for **Si_B-ON(St)** is greater than others (24 kcal mol^{-1}). Comparison of AEs reveals that changes in the interaction energy after employing 10% strain for **Si_N-NO(St)**, **Si_N-ON(St)** and **Si_B-ON(St)** are not significant.

Dispersion-corrected AEs at M05-2X-D3/6–31 ++G(d,p)//M05-2X/6–31+G(d) level of theory for **Si_N-NO(St), Si_N-ON(St)**, **Si_B-NO(St)** and **Si_B-ON(St)** complexes after 10% tensile strain were also calculated. Dispersion-corrected BEs are −25.50, 0.25, −32.35, −9.29 kcal mol^{-1}, respectively. As can be seen, AEs slightly increases upon including the dispersion contribution. Comparison of unstrained and strained dispersion-corrected AEs reveals that their values slightly decrease upon the axial strain.

The results given in Table 4 show that band gap energies of **Si_N-NO(St), Si_N-ON(St)**, **Si_B-NO(St)** and **Si_B-ON(St)** complexes change slightly upon 10% axial strain. The results of the NBO analysis given in

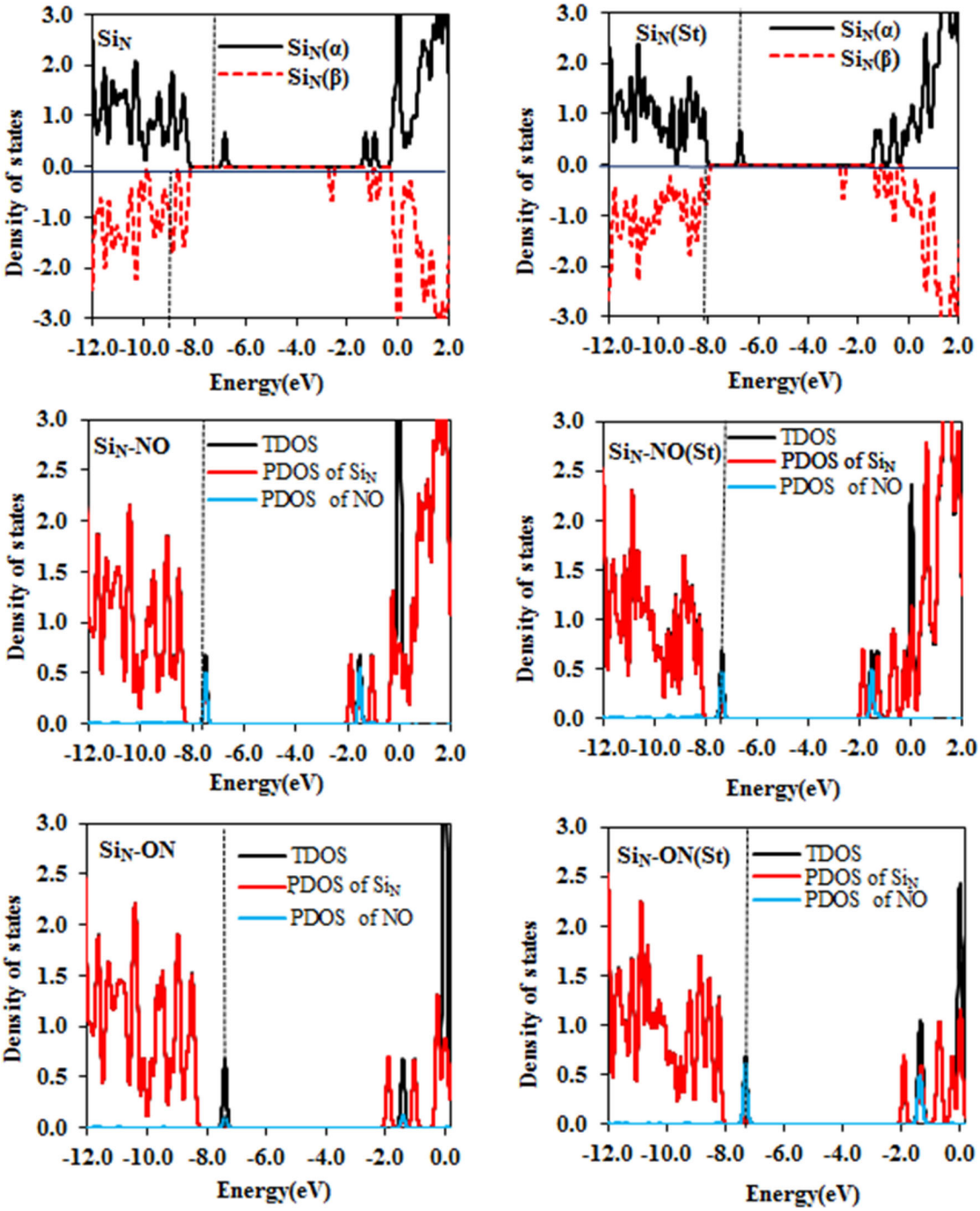

Figure 14 Density of states (DOS) of **Si_N** and **Si_N-NO** complexes. *Black vertical dashed lines* mark the Fermi levels.

Table 4 also show that upon adsorption of NO on the strained NT, a net charge transfer of 0.461, 0.572, 0.487 and 0.600 au occurs from the NT to NO molecule.

DOSs of **Si_N-NO(St), Si_N-ON(St), Si_B-NO(St) and Si_B-ON(St)** complexes are given in Fig. 14. As can be observed, upon adsorption of NO, Fermi level in strained complexes is shifted toward the valence bond and, in turn, band gap increases.

Adsorption of NO on the $Si_{N,B}$ SW-BNNTs

Adsorption of NO on **$Si_{N,B}$**-doped SW-BNNTs was also investigated. The optimized structures are given

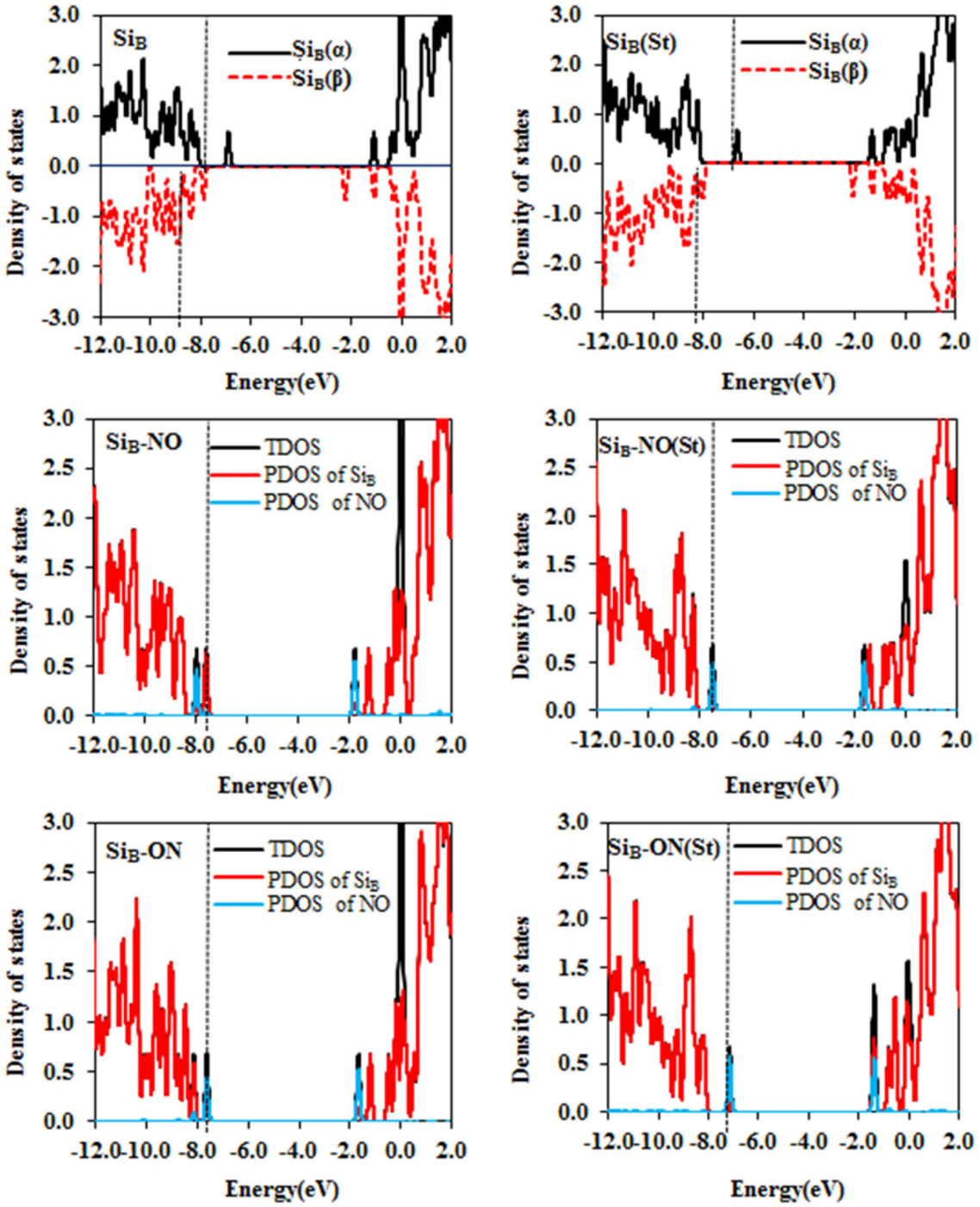

Figure 15 Density of states (DOS) of **Si_B** and **Si_B-NO** complexes. *Black vertical dashed lines* mark the Fermi levels.

in Fig. 13. In **$Si_{N,B}$** SW-BNNT, two vertical N and B atoms were substituted by two Si atoms. Four different configurations were found for **NO-$Si_{N,B}$** SW-BNNT complexes. NO molecule can be attached to either Si → N (Si substituted for N) or Si → B (Si substituted for B) from N and O heads. AEs calculated for unstrained **$Si_{N,B}$-NO1**, **$Si_{N,B}$-ON1**, **$Si_{N,B}$-NO2** and **$Si_{N,B}$-ON2** are −18.78, −33.27, −8.75 and 10.32 kcal mol^{-1}, respectively. It should be noted that in **$Si_{N,B}$-ON1,** NO molecule interacts with Si atoms

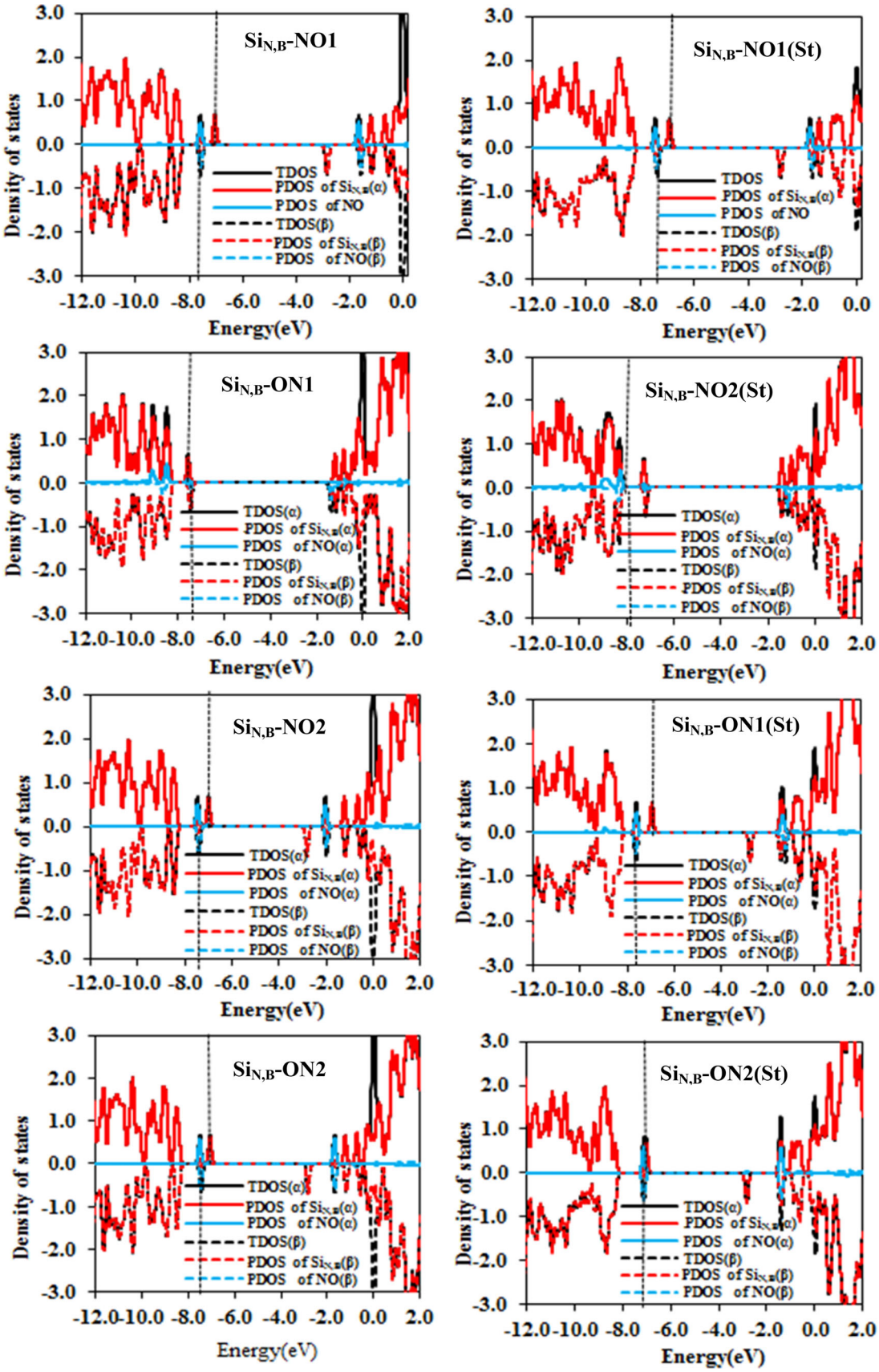
Si$_{N,B}$-NO1
TDOS
PDOS of Si$_{N,B}$(α)
PDOS of NO
TDOS(β)
PDOS of Si$_{N,B}$(β)
PDOS of NO(β)
Density of states
Energy(eV)
Si$_{N,B}$-NO1(St)
Si$_{N,B}$-ON1
TDOS(α)
PDOS of Si$_{N,B}$(α)
PDOS of NO(α)
Si$_{N,B}$-NO2(St)
Si$_{N,B}$-NO2
Si$_{N,B}$-ON1(St)
Si$_{N,B}$-ON2
Si$_{N,B}$-ON2(St)

◀**Figure 16** Density of states (DOS) of $\mathbf{Si_{N,B}}$ and $\mathbf{Si_{N,B}}$**-NO** complexes. *Black vertical dashed lines mark* the Fermi levels.

via O and N atoms and a closed structure is formed. The AE for this cycloaddition configuration is greater than other ones, indicating that cycloaddition configuration of NO-Si-doped SW-BNNT complex is more stable than other ones. After $\mathbf{Si_{N,B}}$**-ON1** complex, $\mathbf{Si_{N,B}}$**-NO1** with AE of −18.78 kcal mol^{-1} is thermodynamically favored. The AE energy of the $\mathbf{Si_{N,B}}$**-ON2** complex in which NO interacts from its O head is positive, suggesting that the formation of Si–O bond in this complex is not thermodynamically favored. These results generally propose that $\mathbf{Si_{N,B}}$ NT can be practically useful for the abstraction of NO molecules.

In order to estimate the magnitude of the dispersion interaction, single-point calculations were carried out using the M05-2X-D3/6-31 ++G(d,p)//M05-2X/6–31+G(d) level of theory. Dispersion-corrected AEs for $\mathbf{Si_{N,B}}$**-NO1**, $\mathbf{Si_{N,B}}$**-ON1,** $\mathbf{Si_{N,B}}$**-NO2** and $\mathbf{Si_{N,B}}$**-ON2** are −19.29, −33.68, −9.22 and 9.85 kcal mol^{-1}, respectively. As can be observed, the change in AEs after dispersion correction is small.

As NO interacts with $\mathbf{Si_{N,B}}$ SW-BNNT, the N–O bond is significantly lengthened. The N–O distance in free NO is 1.145 Å and increases to 1.209, 1,398, 1.214 and 1.310 Å, respectively. As can be seen, a more significant lengthening of NO bond is observed in most stable $\mathbf{Si_{N,B}}$**-ON1** complex. The Si–X (X = N, O or NO) distance in unstrained $\mathbf{Si_{NB}}$**-NO1**, $\mathbf{Si_{N,B}}$**-ON1**, $\mathbf{Si_{N,B}}$**-NO2** and $\mathbf{Si_{N,B}}$**-ON2** complexes is 1.875, 1.744 for Si–N (1.853 for Si–O), 1.785 and 1.721 Å, respectively. The Si–Si bond length in $\mathbf{Si_{N,B}}$ SW-BNNT is 2.245 Å that increases to 2.311, 2.300 and 2.301 Å in $\mathbf{Si_{N,B}}$**-NO1**, $\mathbf{Si_{N,B}}$**-NO2** and $\mathbf{Si_{NB}}$**-ON2** complexes, respectively, with the exception of that of found in most stable $\mathbf{Si_{N,B}}$**-ON1** complex that decreases to 2.226 Å.

NBO analysis shows charge is transferred from NT to NO molecule upon complex formation. The net charge transferred is 0.471, 1.035, 0.506 and 0.631 au, respectively, indicating that charge transfer in most stable complex $\mathbf{Si_{N,B}}$**-ON1** NT is greater than other complexes.

The band gap in $\mathbf{Si_{N,B}}$ is predicted to be 4.85 eV that increases to 5.39, 6.35, 4.96 and 5.36 eV in $\mathbf{Si_{N,B}}$**-NO1**, $\mathbf{Si_{N,B}}$**-ON1**, $\mathbf{Si_{N,B}}$**-NO2** and $\mathbf{Si_{N,B}}$**-ON2** complexes, respectively. The percentage change in the band gap energy is 11.1, 30.9, 2.3 and 10.5, respectively. Therefore, a primary advantage of the change in the band gap of $\mathbf{Si_{N,B}}$ NT upon adsorption is the sensitivity of the 2Si-doped SW-BNNTs toward NO gas. The amount of sensitivity depends on position of NO gas above the NT, and its value is greatest when a closed configuration with the structure of $\mathbf{Si_{N,B}}$**-ON1** is formed. In other words, results of adsorption of NO onto $\mathbf{Si_{N,B}}$ reveal that the Si–Si bond in 2Si-doped SW-BNNTs is highly sensitive to the NO molecule.

To better understand the electronic properties of the complexes, DOSs of unstrained $\mathbf{Si_{N,B}}$**-NO1**, $\mathbf{Si_{N,B}}$**-ON1**, $\mathbf{Si_{N,B}}$**-NO2** and $\mathbf{Si_{N,B}}$**-ON2** complexes were calculated (Fig. 16). As can be seen, $\mathbf{Si_{N,B}}$ NT is a nonmagnetic system, whereas complexes formed from the interaction of NO with NT have magnetic property. Change of magnetic properties upon adsorption of NO can be chiefly used for sensing the amount of NO molecules adsorbed on $\mathbf{Si_{N,B}}$ NT.

Effects of axial strain on the sensitivity of $\mathbf{Si_{N,B}}$ to NO gas are also explored. The most stable structures after adsorption of NO on 10% strained $\mathbf{Si_{N,B}}$ are given in Fig. 13. Four complexes named as $\mathbf{Si_{N,B}}$**-NO1(St)**, $\mathbf{Si_{N,B}}$**-ON1(St)**, $\mathbf{Si_{N,B}}$**-NO2(St)** and $\mathbf{Si_{N,B}}$**-ON2(St)** complexes were found from interaction between $\mathbf{Si_{N,B}}$ and NO gas. The results given in Table 4 show that the NO adsorption properties on the SW-BNNT can be influenced when the B and N atoms of the vertical bond in SW region were substituted with two Si atoms. As can be observed, adsorption energies assessed for $\mathbf{Si_{N,B}}$**-NO1(St)**, $\mathbf{Si_{N,B}}$**-ON1(St)**, $\mathbf{Si_{N,B}}$**-NO2(St)** and $\mathbf{Si_{N,B}}$**-ON2(St)** complexes are −15.73, −27.14, −19.37 and 12.52 kcal mol^{-1}, respectively, indicating that, with the exception of formation of $\mathbf{Si_{N,B}}$**-ON2(St),** adsorption process for other complexes is thermodynamically favored. Comparison of the AEs of strained and unstrained complexes reveals that their values for strained complexes are smaller than unstrained ones, with the exception of $\mathbf{Si_{N,B}}$**-NO2** in which **AE** for it increases from −8.73 to −19.37 kcal mol^{-1} upon the axial strain.

Dispersion-corrected AEs for $\mathbf{Si_{N,B}}$**-NO1(St)**, $\mathbf{Si_{N,B}}$**-ON1(St)**, $\mathbf{Si_{N,B}}$**-NO2(St)** and $\mathbf{Si_{N,B}}$**-ON2(St)** complexes at M05-2X-D3/6-31 ++G(d,p)//M05-2X/6–31+G(d) level of theory are −15.73, −27.14, −19.37 and 12.52 kcal mol^{-1}, respectively, indicating that the adsorption process for formation of strained

complexes is thermodynamically favored, with the exception of **$Si_{N,B}$-ON2(St)**.

The N–O bond is significantly lengthened upon interaction between 10% strained **Si_{NB}** SW-BNNT and NO gas. The N–O distance in free NO is 1.145 Å and increases to 1.213, 1,398, 1.206 and 1.291 Å in **$Si_{N,B}$-NO1(St)**, **$Si_{N,B}$-ON1(St)**, **$Si_{N,B}$-NO2(St)** and **$Si_{N,B}$-ON2(St)** complexes, respectively. As can be seen, same as to that observed in unstrained **$Si_{N,B}$-ON1** complex, a more significant increase in the NO bond length is observed in most stable **$Si_{N,B}$-ON1(St)** complex. The Si–X (X = N, O or NO) distance in strained complexes is 1.845, 1.745 for Si–N (1.856 for Si–O), 1.884 and 1.742 Å, respectively. Comparison of Si–X distances in strained and unstrained complexes shows that the intermolecular distance is lengthened when strained NT interacts with NO gas, with the exception of that observed in **$Si_{N,B}$-NO1(St)** that this distance decreases. The Si–Si bond length in **$Si_{N,B}$** SW-BNNT is 2.245 Å that increases to 2.286, 2.281 and 2.276 Å in **$Si_{N,B}$-NO1(St)**, **$Si_{N,B}$-NO2(St)** and **$Si_{N,B}$-ON2(St)** complexes, with the exception of that of found in the most stable **$Si_{N,B}$-ON1(St)** complex that decreases to 2.207 Å.

The results listed in Table 4 demonstrate that band gap energies of strained **$Si_{N,B}$-NO1(St), $Si_{N,B}$-ON1(St), $Si_{N,B}$-NO2(St) and $Si_{N,B}$-ON2(St)** are 5.20, 5.86, 5.52 and 5.58 eV, respectively. As can be seen, band gap energies for **$Si_{N,B}$-NO1(St), $Si_{N,B}$-ON1(St)** complexes decrease and those of **$Si_{N,B}$-NO2(St)** and **$Si_{N,B}$-ON2(St)** ones increase compared with unstrained complexes. The results of the NBO analysis given in Table 4 show that upon adsorption of NO on the strained NT, a net charge of 0.490, 1.044, 0.196 and 0.010 au is transferred from the NT to NO molecule. There is a correlation between band gap energies and charge transfer values so that decrease/increase in band gap energies upon axial strain is accompanied with increase/decrease in charge transfer values.

To gain a better insight about the electronic properties of the complexes, DOSs of unstrained **$Si_{N,B}$-NO1(St), $Si_{N,B}$-ON1(St), $Si_{N,B}$-NO2(St) and $Si_{N,B}$-ON2(St)** complexes are calculated and given in Fig. 16. As can be seen, DOS of strained complexes is same as the unstrained complexes. Strained **$Si_{N,B}$** NT is a nonmagnetic system and is converted to magnetic systems when interacts with the NO gas. Change of magnetic properties upon the interaction of NO can be principally used for sensing the amount of NO molecules adsorbed on strained **$Si_{N,B}$** NT.

Conclusions

The M05-2X density functional theory was employed to investigate the effect of the Si doping defect on the properties of (6,0) SW-BNNT under the axial strain. The calculated binding energy for Si-doped SW defective BNNTs is smaller than SW defective BNNT. In Si-doped SW–BNNT, the defect region serves as a nucleation site for fraction. In general, order of stability of Si-doped SW defective BNNTs is **Si_N** > **Si_B** > **$Si_{N,B}$**. During axial strain, the formation energy of these NTs increases. The band gap energies, dipole moment, chemical potential, chemical hardness and softness, electrophilicity index, radial buckling and the maximum amount of electronic charge for Si-doped SW–BNNTs were also calculated. Order of energy gap is SW-BNNT > **Si_B** > **Si_N** > **$Si_{N,B}$**. From a comparison of energy gaps, it can be concluded that the conductivity of **$Si_{B,N}$** NT is greater and excitation energy of **$Si_{B,N}$** NT is smaller than other two NTs. The band gap decreases upon axial strain for **Si_B** and **Si_N** models, and it almost remains constant in **$Si_{N,B}$** model in low tensile strain.

In the second part of this work, sensitivity of strained and unstrained Si-doped SW-BNNTs toward NO gas is evaluated. The results show that the chemical adsorption of NO in many states is thermodynamically favored in both strained and unstrained Si-doped NTs. Thus, it is expected that Si-doped SW-BNNTs could be a favorable gas sensor for sensing the NO molecule.

Compliance with ethical standards

Conflict of interest No potential conflict of interest is reported by the authors.

References

[1] Rubio A, Corkill JL, Cohen ML (1994) Theory of graphitic boron nitride nanotubes. Phys Rev B 49(7):5081–5084

[2] Chopra NG, Luyken RJ, Cherrey K, Crespi VH, Cohen ML, Louie SG, Zettl A (1995) Boron nitride nanotubes. Science 269(269):966–967

[3] Wildoer JWG, Venema LC, Rinzler AG, Smalley RE, Dekker C (1998) Boron nitride nanotubes. Nature 391:59

[4] Blase X, Rubio A, Louie SG, Cohen ML (1994) Stability and band gap constancy of boron nitride nanotubes. Europhys Lett 28:335

[5] Fuentes GG, Borowiak-Palen E, Pichler T, Liu X, Gra A, Behr G, Kalenczuk J, Knupfer M, Fink J (2003) Electronic structure of multiwall boron nitride nanotubes. Phys Rev B 67(3):035429

[6] Zhi C, Bando Y, Tang C, Golberg D (2010) Boron nitride nanotubes. Mater Sci Eng R 70:92–111

[7] Freitas A, Azevedo S, Kaschny JR (2013) Effects of a transverse electric field on the electronic properties of single- and multi-wall BN nanotubes. Solid State Commun 153:40–45

[8] Roohi H, Bagheri S (2013) Effect of axial strain on structural and electronic properties of zig-zag type of boron nitride nanotube (BNNT): a quantum chemical study. Struct Chem 24(1):409–420

[9] Zhukovskii YF, Piskunov S, Begens J, Kazerovskis J, Lisovski O (2013) First-principles calculations of point defects in inorganic nanotubes. Phys Status Solidi 250:793–800

[10] Silva L, Guerini S, Lemos V, Filho J (2006) Electronic and structural properties of oxygen doped BN nanotubes. IEEE Trans Nanotechnol 5:517–522

[11] Liu H, Turner CH (2014) Adsorption properties of nitrogen dioxide on hybrid carbon and boron-nitride nanotubes. Phys Chem Chem Phys 16:22853–22860

[12] Zhao JX, Ding YH (2008) Theoretical study of Ni adsorption on single-walled boron nitride nanotubes with intrinsic defects. J Phys Chem C 112:5778–5783

[13] Xie Y, Zhang JM (2011) First-principles study on substituted doping of BN nanotubes by transition metals V, Cr and Mn. Comput Theor Chem 976:215–220

[14] Tang C, Bando Y, Huang Y, Yue SL, Gu CZ, Xu FF (2005) Fluorination and electrical conductivity of BN nanotubes. J Am Chem Soc 127:6552–6553

[15] Stephan O, Ajayan PM, Colliex C, Redlich P, Lambert JM, Bernier P, Lefin P (1994) Doping graphitic and carbon nanotube structures with boron and nitrogen. Science 266:1683–1685

[16] Golberg D, Bando Y, Dorozhkin P, Dong ZC (2004) Synthesis, analysis, and electrical property measurements of compound nanotubes in the B-C-N ceramic system. MRS Bull 29:38–42

[17] Ci L, Song L, Jin C, Jariwala D, Wu D, Li Y, Srivastava A, Wang ZF, Storr K, Balicas L, Liu F, Ajayan PM (2010) Atomic layers of hybridized boron nitride and graphene domains. Nat Mater 9:430–435

[18] Krivanek OL, Chisholm MF, Nicolosi V, Pennycook TJ, Corbin GJ, Dellby N, Murfitt MF, Own CS, Szilagyi ZS, Oxley MP, Pantelides ST, Pennycook SJ (2010) Atom-by-atom structural and chemical analysis by annular dark-field electron microscopy. Nature 464:571–574

[19] Wei X, Wang M, Bando Y, Golberg D (2010) Post-synthesis carbon doping of individual multiwalled boron nitride nanotubes via electron-beam irradiation. J Am Chem Soc 132:13592–13593

[20] Wei X, Wang M, Bando Y, Golberg D (2011) Electron-beam-induced substitutional carbon doping of boron nitride nanosheets, nanoribbons, and nanotubes. ACS Nano 5:2916–2922

[21] Tontapha S, Morakot N, Ruangpornvisuti V, Wanno B (2012) Geometries and stabilities of transition metals doped perfect and Stone-Wales defective armchair (5,5) boron nitride nanotubes. Struct Chem 23:1819–1830

[22] Roohi H, Jahantab M, Rahmdel Delcheh S, Pakdel Khoshakhlagh B (2015) Chemical functionalization of boron nitride nanotube via the 1,3-dipolar cycloaddition reaction of azomethine ylide: a quantum chemical study. Struct Chem 26:749–759

[23] Roohi H, Khyrkhah S (2015) Green chemical functionalization of single-wall carbon nanotube with methylimidazolium dicyanamid ionic liquid: a first principle computational exploration. J Mol Liq 211:498–505

[24] Roohi H, Maleki L (2016) Effects of C1-3-doping on electronic and structural properties of stone wales defective boron nitride nanotubes as well as their NO gas sensitivity. RSC Adv 6:11353–11369

[25] Kim G, Park J, Hung S (2012) First principle study of substitutional carbon pair and Ston-Wals defect complexes in boron nitride nanotubes. Chem Phys Lett 522:79–82

[26] Chen YK, Liu LV, Wang YA (2010) Density functional study of interaction of atomic Pt with pristine and stone-wales-defective single-walled boron nitride nanotubes. J Phys Chem C 114:12382–12388

[27] Wang R, Zhu R, Zhang D (2008) Adsorption of formaldehyde molecule on the pristine and silicon-doped boron nitride nanotubes. Chem Phys Lett 467:131–135

[28] Stone AJ, Wales DJ (1986) Theoretical studies of icosahedral C60 and some related species. Chem Phys Lett 128:501–503

[29] Kumar R, Parashar A (2016) Atomistic modeling of BN nanofillers for mechanical and thermal properties: a review. Nanoscale 8:22

[30] Dumitrica T, Yakobson BI (2005) Rate theory of yield in boron nitride nanotubes. Phys Rev B 72:035418

[31] Choi J, Pyo S, Baek DH, Lee JI, Kim J (2014) Thickness, alignment and defect tunable growth of carbon nanotube arrays using designed mechanical loads. Carbon 66:126–133

[32] Miyamoto Y, Rubio A, Berber S, Yoon M, Toanek D (2004) Spectroscopic characterization of Stone-Wales defects in nanotubes. Phys Rev B 691:21413

[33] Bettinger HF, Dumitrica T, Scuseria GE, Yakobson BI (2002) Mechanically induced defects and strength of BN nanotubes. Phys Rev B 65:041406

[34] Roohi H, Jahantab M, Yakta M (2015) Effect of the Stone-Wales (SW) defect on the response of BNNT to axial tension and compression: a quantum chemical study. Struct Chem 26:11–22

[35] Li Y, Zhou Z, Golberg D, Bando Y, von Rague Scheyer P, Chen Z (2008) Stone-Wales defects in single-walled boron nitride nanotubes: formation energies, electronic structures, and reactivity. J Phys Chem C 112:1365–1370

[36] An W, Wu X, Yang JL, Zeng XC (2007) Adsorption and surface reactivity on single-walled boron nitride nanotubes containing Stone-Wales defects. J Phys Chem C 111:14105–14112

[37] Umadevi P, Aiswarya T, Senthilkumar L (2015) Encapsulation of fluoroethanols in pristine and Stone-Wales defect boron nitride nanotube—A DFT study. Appl Surf Sci 345:369–378

[38] Tabtimsai C, Nonsri A, Gratoo N, Massiri N, Suvanvapee P, Wanno B (2014) Carbon monoxide adsorption on carbon atom doped perfect and Stone-Wales defect single-walled boron nitride nanotubes: a DFT investigation. Monatsh Chem 145:725–735

[39] Gupta SK, He H, Banyai D, Si M, Pandey R, Karna SP (2014) Effect of Si doping on the electronic properties of BN monolayer. Nanoscale 6:5526–5531

[40] Wei X, Wang MS, Bando Y, Golberg D (2010) Tensile tests on individual multi-walled boron nitride nanotubes. Adv Mater 22:4895–4899

[41] Liao ML, Wang YC, Ju SP, Lien TW, Huang LF (2011) Deformation behaviors of an armchair boron-nitride nanotube under axial tensile strains. J Appl Phys 110:054310

[42] Ge C, Li X, Dong J (2011) Electronic structures of deformed B2C nanotubes under tensile strain. Phys E 44:105–110

[43] Deng ZY, Zhang JM, Xu KW (2016) Adsorption of SO2 molecule on doped (8,0) boron nitride nanotube: a first-principles study. Phys E 76:47–51

[44] Lin S, Ye X, Huang J (2015) Can metal-free silicon-doped hexagonal boron nitride nanosheet and nanotube exhibit activity toward CO oxidation? Phys Chem Chem Phys 17:888–895

[45] Esrafili MD, Saeidi N (2015) Si-embedded boron-nitride nanotubes as an efficient and metal-free catalyst for NO oxidation. Superlattices Microstruct 81:7–15

[46] Zhang J, Zhang Y, Pan Z, Yang S, Shi J, Li S, Min D, Li X, Wang X, Liu D, Yang A (2015) Properties of a weakly ionized NO gas sensor based on multi-walled carbon nanotubes. Appl Phys Lett 107:093104–093105

[47] You X, Huo YP, Zhang JM (2012) First-principles study of CO and NO adsorption on transition metals doped (8,0) boron nitride nanotube. Appl Surf Sci 258:6391–6397

[48] Bezi Javan M (2015) Adsorption of CO and NO molecules on SiC nanotubes and nanocages. Surf Sci 635:128–142

[49] Zhao Y, Truhlar DG (2006) A new local density functional for main-group thermochemistry, transition metal bonding, thermochemical kinetics, and noncovalent interactions. J Chem Phys 125:194101

[50] Zhao Y, Truhlar DG (2008) The M06 suite of density functionals for main group thermochemistry, thermochemical kinetics, noncovalent interactions, excited states, and transition elements: two new functionals and systematic testing of four M06-class functionals and 12 other functionals. Theor Chem Acc 120:215–241

[51] Frisch MJ, Trucks GW, Schlegel HB, Scuseria GE, Rob MA, Cheeseman JR, Montgomery Jr JA, Vreven T, Kudin KN, Burant JC, Millam JM, Iyengar SS, Tomasi J. Barone V, Mennucci B, Cossi M, Scalmani G, Rega N, Petersson GA, Nakatsuji H, Hada M, Ehara M, Toyota K, Fukuda R, Hasegawa J, Ishida M, Nakajima T, Honda Y, Kitao O, Nakai H, Klene M, Li X, Knox JE, Hratchian HP, Cross JB, Bakken V, Adamo C, Jaramillo J, Gomperts R, Stratmann RE, Yazyev O, Austin AJ, Cammi R, Pomelli C, Ochterski JW, Ayala PY, Morokuma K, Voth GA Salvador P, Dan-nenberg JJ, Zakrzewski VG, Dapprich S, Daniels AD, Strain MC, Farkas O, Malick DK, Rabuck AD, Raghavachari K, Foresman JB, Ortiz JV, Cui Q, Baboul AG, Clifford S, Cioslowski J, Stefanov BB, Liu G, Liashenko A, Piskorz P, Komaromi I, Martin RL, Fox DJ, Keith T, Al-Laham MA, Peng CY, Nanayakkara A, Challacombe M, Gill PMW, Johnson B, Chen W, Wong MW, Gonzalez C, Pople JA (2004) Gaussian 03, Revision E.01, Gaussian, Inc., Wallingford CT

[52] Schmidt MW, Baldridge KK, Boatz JA, Elbert ST, Gordon MS, Jensen JH, Koseki S, Matsunaga N, Nguyen KA, Su S, Windus TL, Dupuis M, Montgomery JA (1993) General atomic and molecular electronic structure system. J Comput Chem 14:1347–1363

[53] Beer FP, Johnston ER, Dewolf JT (2006) Mechanics of materials, vol 54. McGraw-Hill Education, New York

[54] Lu T, Chen F (2012) A multifunctional wavefunction analyzer: multiwfn. J Comput Chem 33:580–592

[55] Neamen DA (2011) Semiconductor physics and devices basic principles, vol 784, 4 th edn. McGraw-Hill, New York

[56] Parr RG, Yang W (1989) Density functional theory of atoms and molecules. Oxford University Press, New York

[57] Geerlings P, Proft FD, Langenaeker W (2003) Conceptual density functional theory. Chem Rev 103:1793–1874

[58] Roy RK, Saha S (2010) Studies of regioselectivity of large molecular systems using DFT based reactivity descriptors. Annu Rep C 106:106–118

[59] Gyftopoulos EP, Hatsopoulos GN (1968) Quantum-thermodynamic definition of electronegativity. Proc Natl Acad Sci USA 60:786–793

[60] Parr RG, Donnelly RA, Levy M, Palke WE (1978) Electronegativity-the density functional viewpoint. J Chem Phys 68:3801–3807

[61] Parr RG, Pearson RG (1983) Absolute hardness: companion parameter to absolute electronegativity. J Am Chem Soc 105:7512–7516

[62] Parr RG, Szentpály L, Liu S (1999) Electrophilicity index. J Am Chem Soc 121:1922–1924

[63] Si MS, Xue DS (2006) First-principles study of silicon-doped (5,5) BN nanotubes. Europhys Lett 76:664–669

[64] Cho YJ, Kim CH, Kim HS, Park J, Choi HC, Shin HJ, Gao G, Kang HS (2009) Electronic structure of Si-doped BN nanotubes using X-ray photoelectron spectroscopy and first-principles calculation. Chem Mater 21:136–143

[65] Liu YJ, Gao B, Xu D, Wang H, Zhao J (2014) Theoretical study on Si-doped hexagonal boron nitride (h-BN) sheet: electronic, magnetic properties, and reactivity. Phys Lett A 378:2989–2994

[66] Ju SP, Wang YC, Lien TW (2011) Tuning the electronic properties of boron nitride nanotube by mechanical uni-axial deformation: a DFT study. Nanoscale Res Lett 6:160

[67] Guerini S, Kar T, Piquini P (2004) Theoretical study of Si impurities in BN nanotubes. Eur Phys J B 38:515

[68] Tang CC, Bando Y, Ding XX, Qi SR, Golberg D (2002) Catalyzed collapse and enhanced hydrogen storage of BN nanotubes. J Am Chem Soc 124:14550–14551

[69] Gao G, Seok Kang H (2008) First principles study of NO and NNO chemisorption on silicon carbide nanotubes and other nanotubes. J Chem Theory Comput 4:1690–1697